

Measurements of inclusive  $J/\psi \rightarrow \mu\mu$  in  $p+p$ ,  
 $p+\text{Al}$ ,  $p+\text{Au}$ , and  ${}^3\text{He}+\text{Au}$  collisions at  
 $\sqrt{s_{NN}} = 200 \text{ GeV}$

Matt Durham, Sanghoon Lim  
 Los Alamos National Laboratory

September 16, 2018

## Contents

<b>1</b>	<b>Introduction</b>	<b>3</b>
<b>2</b>	<b>Run QA</b>	<b>4</b>
2.1	Run QA	4
2.2	MuID-2D trigger livetime	4
<b>3</b>	<b>Acceptance and efficiency</b>	<b>10</b>
3.1	MuID tube efficiency	10
3.2	Comparison of MuID-1D trigger efficiency	21
3.3	MuTr efficiency	25
3.4	Simulation procedure	26
3.5	BBCLL1 rate dependent efficiency correction	26
3.6	MuID-2D trigger efficiency	36
3.7	Acceptance and reconstruction efficiency	47
3.8	Comparison between GEANT3 and GEANT4	55
<b>4</b>	<b>Fit</b>	<b>56</b>
4.1	Cuts	56
4.2	Like-sign Background	56
4.3	Fit	56
4.4	Run-14 ${}^3\text{He}+\text{Au}$	57
4.5	Run-15 $p+\text{Al}$	57
4.6	Run-15 $p+\text{Au}$	60
4.7	Fit results	60

<b>5</b>	<b>Systematic uncertainty</b>	<b>63</b>
5.1	Fit . . . . .	63
5.2	Run-to-run variation . . . . .	66
5.3	Acceptance and reconstruction efficiency . . . . .	66
5.4	Trigger efficiency . . . . .	69
5.5	$J/\psi$ polarization . . . . .	72
<b>6</b>	<b>Results</b>	<b>76</b>
6.1	$dN/dy$ of $J/\psi$ . . . . .	76
6.2	$R_{pA}$ of $J/\psi$ . . . . .	78

# 1 Introduction

This Note describes the measurement of the  $J/\psi$  cross section at forward and backward rapidity, through the decays to dimuons, from the Run-14  $^3\text{He}+\text{Au}$  and Run-15  $p+p$ ,  $p+\text{Al}$  and  $p+\text{Au}$  data.

The analysis proceeds as follows: First, a set of criteria are applied to the various data sets to determine a good runs list for each arm in each data set. From these good runs, the dimuon invariant mass spectrum is prepared using tracks that are measured in the muon arms, in eight different rapidity bins for each beam species. The ROOT likelihood fitter is then used to fit the invariant mass spectrum from the Run-15  $p+p$  data with a sum of combinatorial background, correlated background, and two peaks which represent the  $J/\psi$  and  $\psi(2S)$  charmonium states. The line shape of the peaks (specifically the  $\alpha$  and  $n$  Crystal Ball parameters describing the low-side tail) are determined from these fits to the  $p+p$  data, and then fixed to these values while fitting the ion data sets. The integrals of these peak shapes are extracted from the fits and are shown in Tab. 6. Corrections for the luminosity dependent acceptance $\times$ efficiency of the PHENIX muon arms are applied, and the result is divided by the sampled luminosity to determine a production cross section. Systematic uncertainties are determined by varying the peak shapes, background normalization, and acceptance $\times$ efficiency and trigger efficiency corrections.

## 2 Run QA

### 2.1 Run QA

Basic run QA had been done in the previous study for PPG188 and described in AN1240. Additional QA with the trigger livetime described in the following section is done for invariant yield. The list of bad runs can be found here.

[https://www.phenix.bnl.gov/WWW/p/draft/shlim/Run14Run15\\_inclusive\\_jpsi/](https://www.phenix.bnl.gov/WWW/p/draft/shlim/Run14Run15_inclusive_jpsi/)

### 2.2 MuID-2D trigger livetime

Figures 1, 2, 3, and 4 show the correlation of trigger livetime between the MuID-2D and MB triggers in three data sets. Depending on trigger configuration like which BBCLL1 trigger is coincidence with the MuID-2D trigger and pre-scale, the trigger livetime of MuID-2D trigger becomes smaller than that of the BBCLL1 trigger. In case of the Run-15  $p+p$ , it shows lowest relative livetime of the MuID-2D trigger. In order to check whether this lower live time affects the yield calculation, raw yield of  $J/\psi$  candidates as a function of relative livetime of the MuID-2D trigger is compared before and after the livetime correction for normalization as shown in Fig. 5. After correction, the trend of raw yield as a function of correction factor looks affected by over-correction, because a good correction should make the corrected distributions flat. The 10% level of yield drop shown in the top panel can be explained by beam instant luminosity dependent detector efficiency, as the relative MuID-2D livetime decrease with increasing BBCLL1 trigger rate. Another check is done with the MuID-2D trigger efficiency with  $J/\psi$  candidates MB triggered event sample. By assuming the drop of relative MuID-2D trigger livetime is due to the MuID-2D trigger, one can expect a lower trigger efficiency with the live trigger bit than a trigger efficiency with the raw trigger bit. However, we observed exactly same trigger efficiency between with the live trigger bit and with the raw trigger bit which agrees with the conclusion from the study of raw yield of  $J/\psi$  candidates shown in Fig. 5. Therefore, it is decided not to correct the lower livetime of MuID-2D trigger, but runs showing a very low livetime ( $< 0.3$ ) are rejected in this analysis.

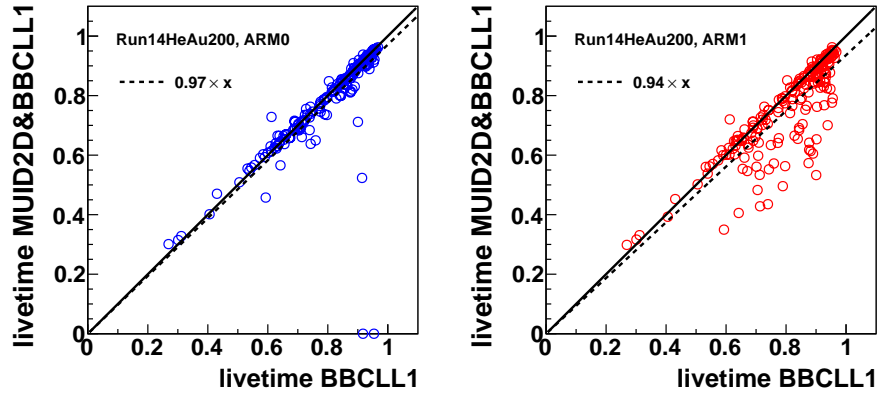


Figure 1: Correlation of trigger livetime between the MuID-2D and MB triggers in Run-14  $^3\text{He}+\text{Au}$  run.

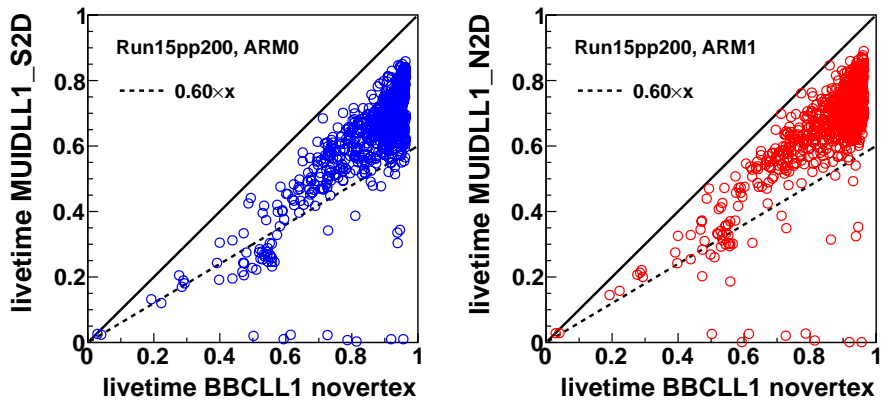


Figure 2: Correlation of trigger livetime between the MuID-2D and MB triggers in Run-15  $p+p$  run.

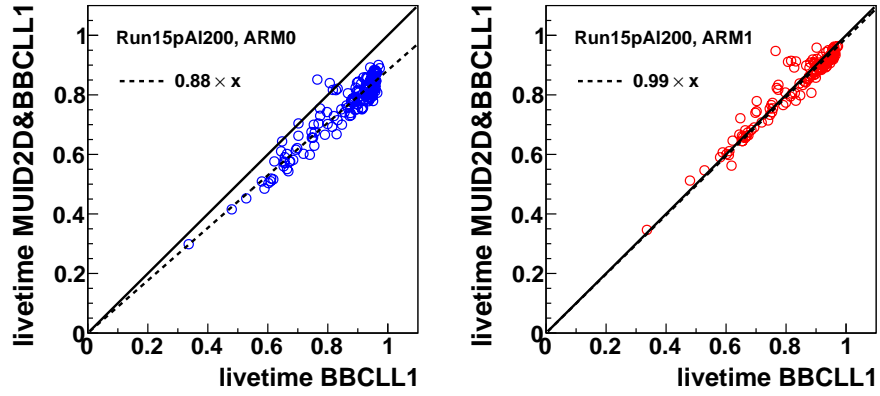


Figure 3: Correlation of trigger livetime between the MuID-2D and MB triggers in Run-15  $p$ +Al run.

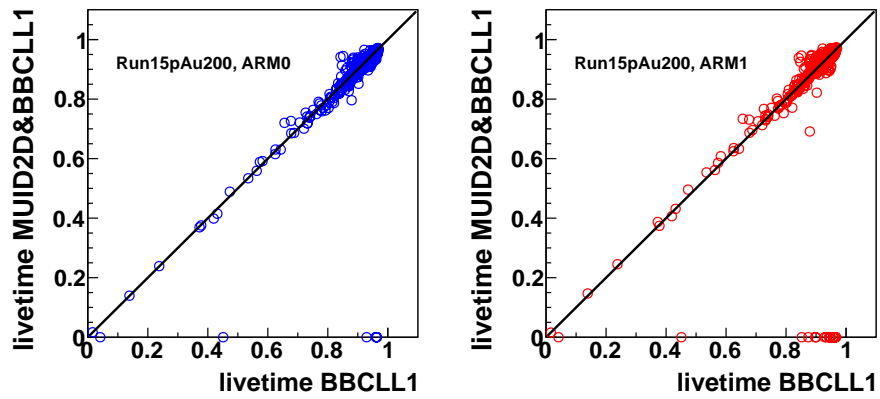


Figure 4: Correlation of trigger livetime between the MuID-2D and MB triggers in Run-15  $p$ +Au run.

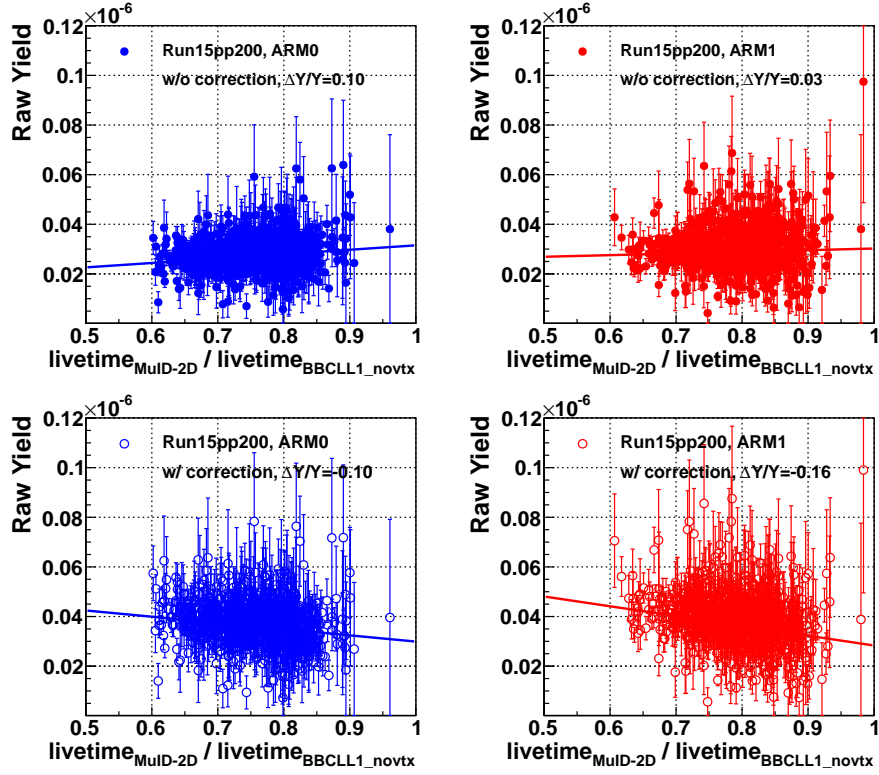


Figure 5: Comparison of raw yield of  $J/\psi$  candidates as a function of relative livetime of the MuID-2D trigger before (top) and after (bottom) correction in Run-15  $p+p$  run.

Additional check has been done is to compare raw  $J/\psi$  yield between the MuID-1D and the MuID-2D triggered events. Figure 6 shows the correlation between the MuID-1D and MB triggers in Run-15  $p+p$  run, and they're quite consistent unlike the MuID-2D trigger. Since the acceptance and reconstruction efficiency of  $J/\psi$  will be independent on triggers, so raw yield can be compared by applying the trigger efficiency and the prescale corrections. If there's a rejection of signal events triggered by the MuID-2D trigger due to the lower livetime, we can expect a lower raw yield of  $J/\psi$  in the MuID-2D triggered events. Figure 7 shows a comparison as a function of  $J/\psi$  rapidity, and the ratio of raw yields clearly indicate that the livetime correction is unnecessary.

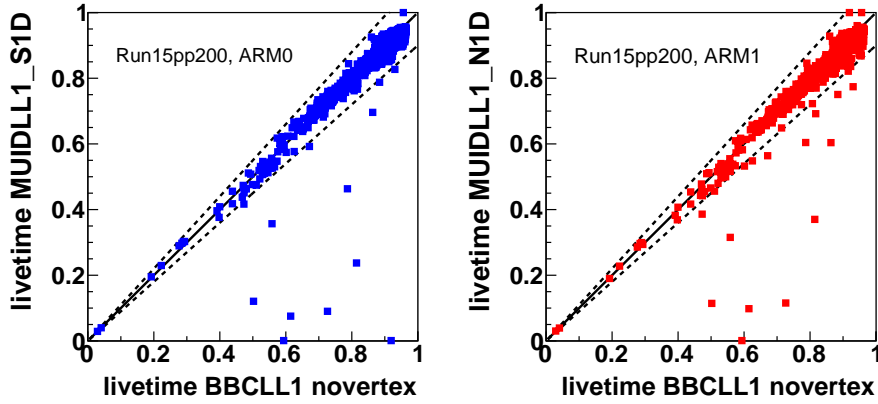


Figure 6: Correlation of trigger livetime between the MuID-1D and MB triggers in Run-15  $p+p$  run.

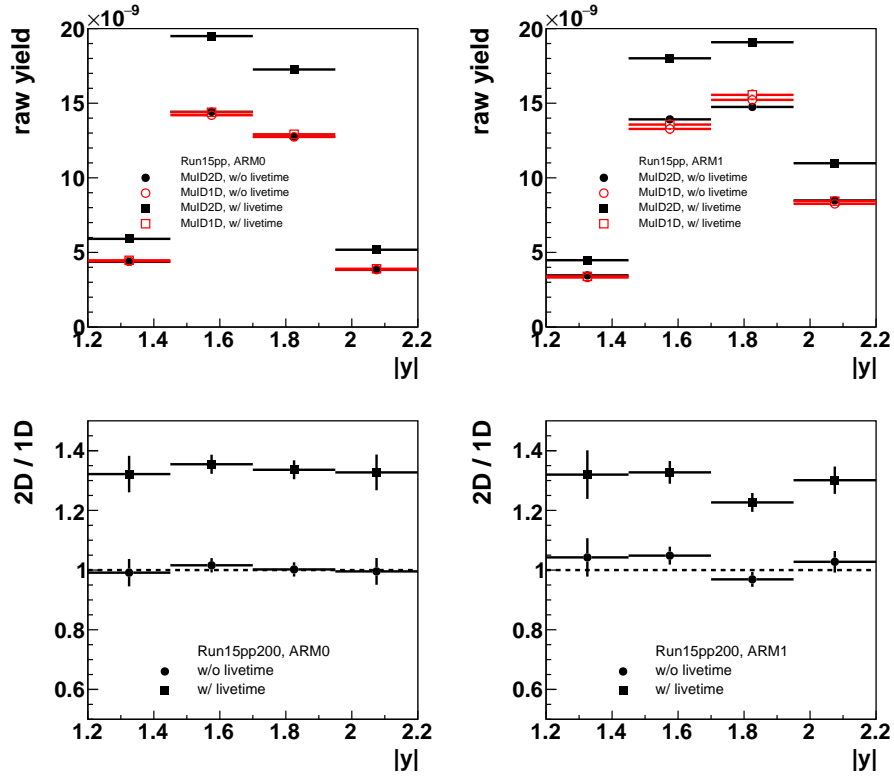


Figure 7: Comparison of raw yield of  $J/\psi$  between the MuID-1D and MuID-2D triggered data in Run-15  $p+p$ .

## 3 Acceptance and efficiency

### 3.1 MuID tube efficiency

The data driven method (**offline/analysis/muideff**) has been usually used to evaluate the MuID tube efficiency. In this method, ntuple files containing good MuID tracks are used. In case of data sets of small collision systems which usually use Muon/MuID triggers to enrich track samples in the muon arms, most of MuID tracks used for the MuID tube efficiency evaluation are from events triggered by triggers coincidence with the MuID triggers. Depending on how tight the trigger requirement is, the purity of MuID track samples can be different between events from MB and MuID triggers. Since it is hard to analyze MB and MuID triggered events separately with the currently used ntuple files, a new framework using picoDST files has been introduced.

Figure 10 show the average MuID tube efficiency of each plane as a function of BBCLL1 novertex trigger rate with muon triggered events in Run-15  $p$ +Au, and each data point represent each run. Fig. 11 show the same plots with MB triggered events. They look generally quite similar, but there are visible differences in high BBCLL1 novertex rate where the MuID tube efficiency becomes lower. Fig. 12 show the ratio of average MuID tube efficiency between MB and muon triggered events, and the deviation increases as BBCLL1 novertex rate increases (true MuID tube efficiency decreases). This comparison show there is a non-negligible trigger bias in the MuID tube efficiency evaluation, and it is more important when the true MuID efficiency gets lower ( $\sim 10\%$  bias in  $\sim 70\%$  of MuID tube efficiency). It is ideal to evaluate the MuID tube efficiency only with MB triggered events, but the statistic is quite limited. Therefore, a bias correction factor is evaluated like fitting the ratio shown in Fig. 12 and applied to the MuID tube efficiency evaluated with muon triggered events. Fig. 13, 14, and 15 show same plots in Run-15  $p$ +Al, the trigger bias in  $p$ +Al data is smaller than that in  $p$ +Au data. Fig. 16 show the MuID tube efficiency in Run-14  $^3\text{He}$ +Au with MB triggered events. Since only MuID-2D triggers were used in the Run-14  $^3\text{He}$ +Au data taking, so the MuID tube efficiency evaluated with MB triggered events is directly used.

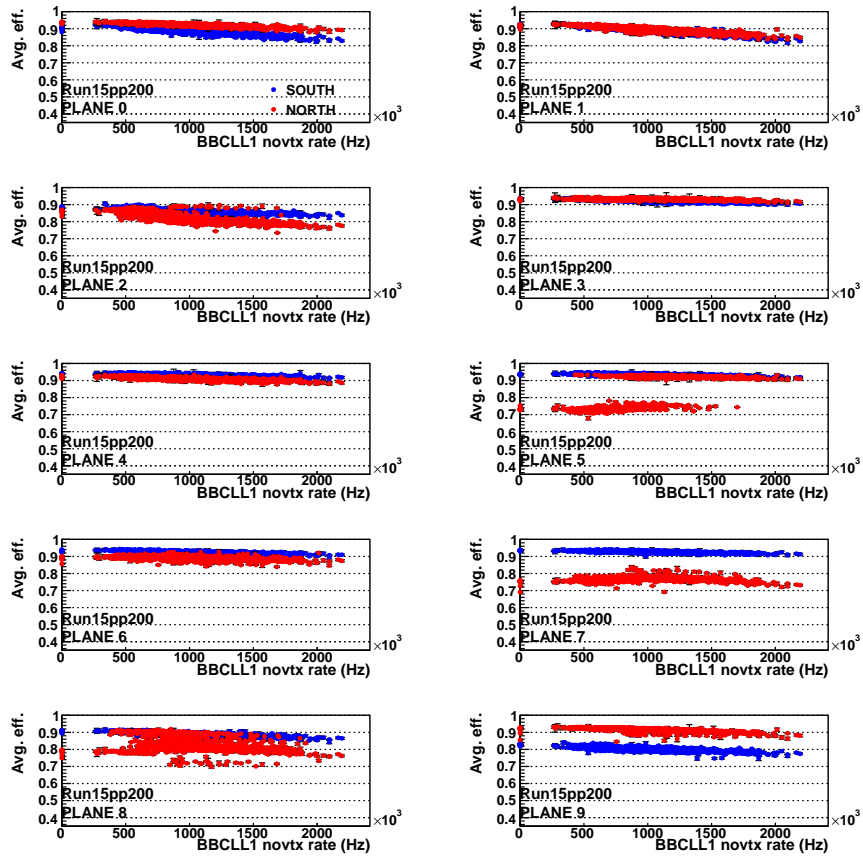


Figure 8: Average MuID tube efficiency of each plane as a function of BBCLL1 novertex trigger rate with muon triggered events in Run-15  $p+p$ .

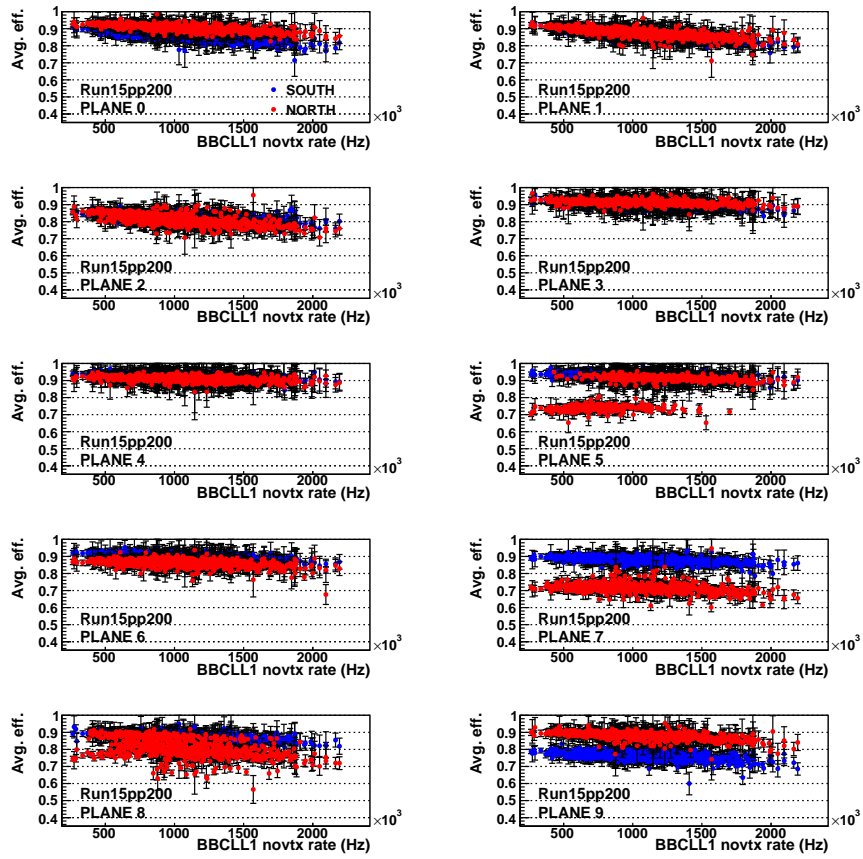


Figure 9: Average MuID tube efficiency of each plane as a function of BBCLL1 novertex trigger rate with MB triggered events in Run-15  $p+p$ .

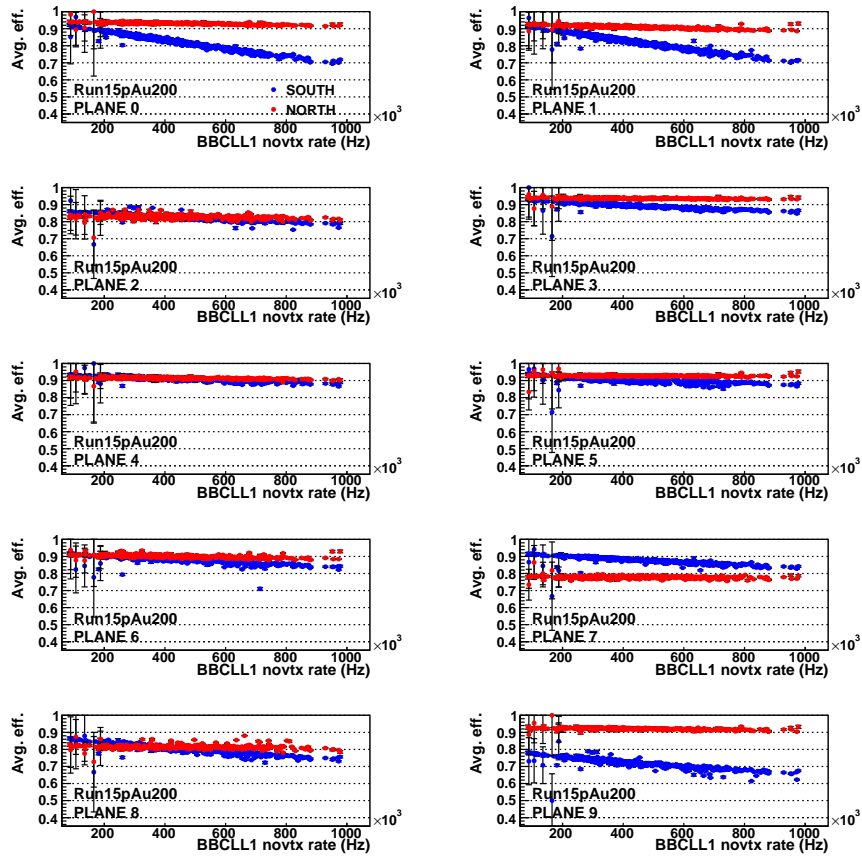


Figure 10: Average MuID tube efficiency of each plane as a function of BBCLL1 novertex trigger rate with muon triggered events in Run-15  $p+Au$ .

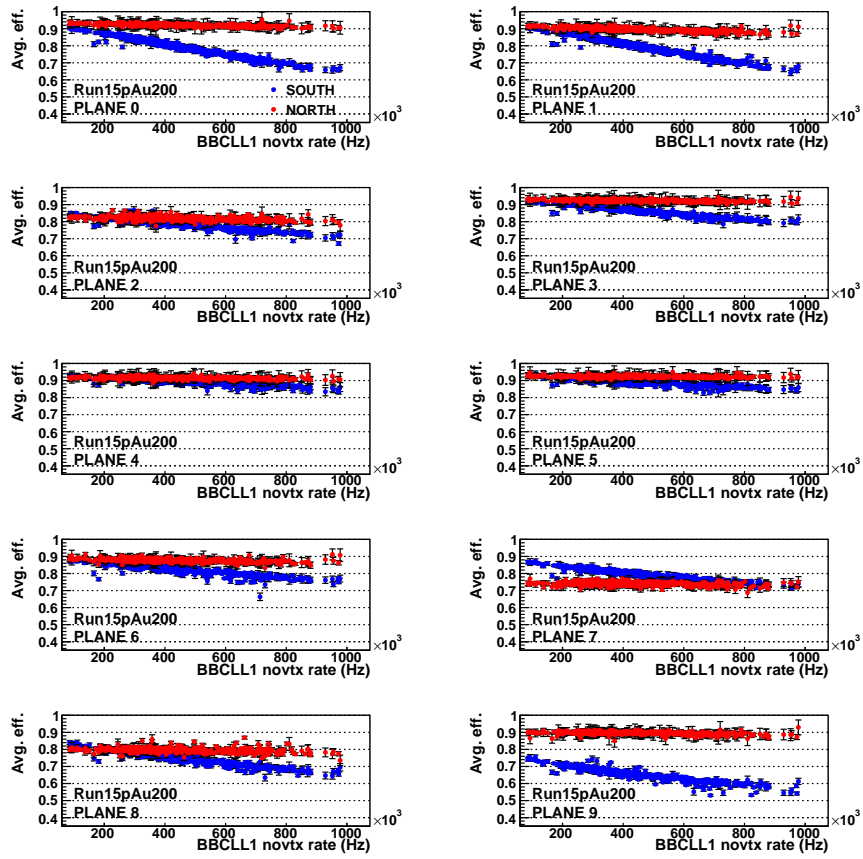


Figure 11: Average MuID tube efficiency of each plane as a function of BBCLL1 novertex trigger rate with MB triggered events in Run-15  $p+Au$ .

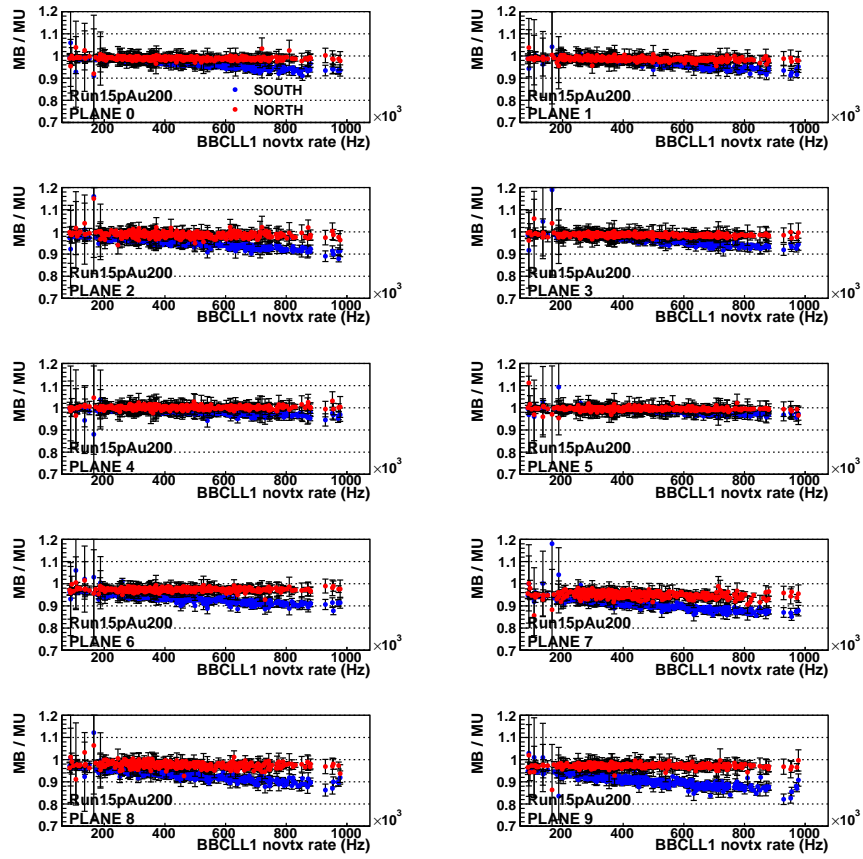


Figure 12: Comparison of average MuID tube efficiency of each plane as a function of BBCL1 novertex trigger rate in Run-15  $p+Au$ .

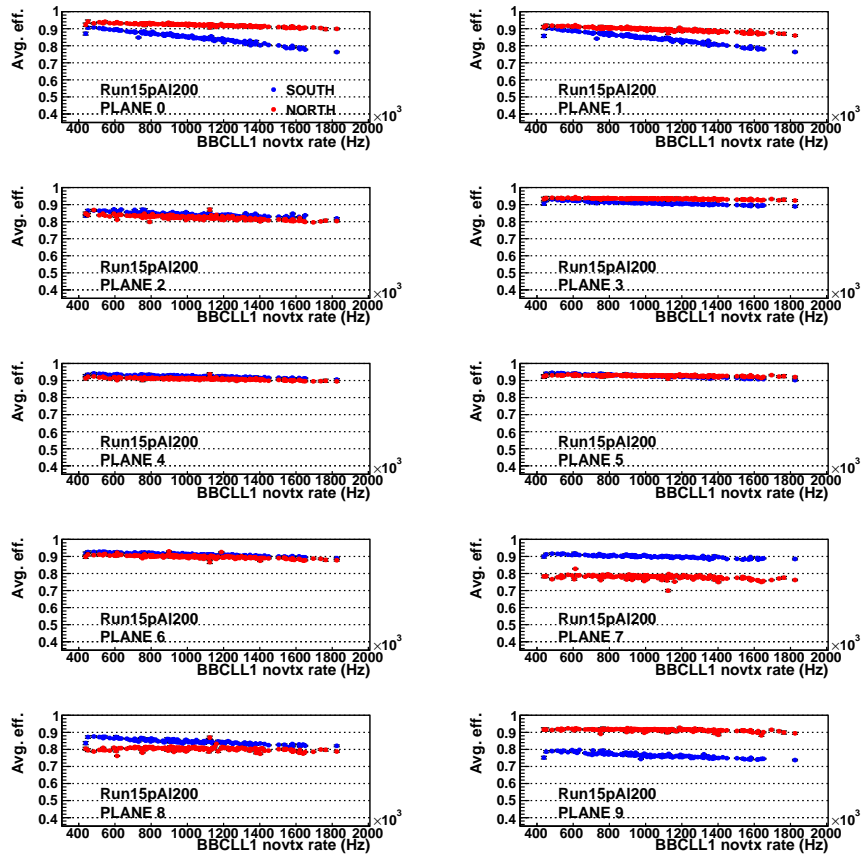


Figure 13: Average MuID tube efficiency of each plane as a function of BBCLL1 novertex trigger rate with muon triggered events in Run-15  $p+Al$ .

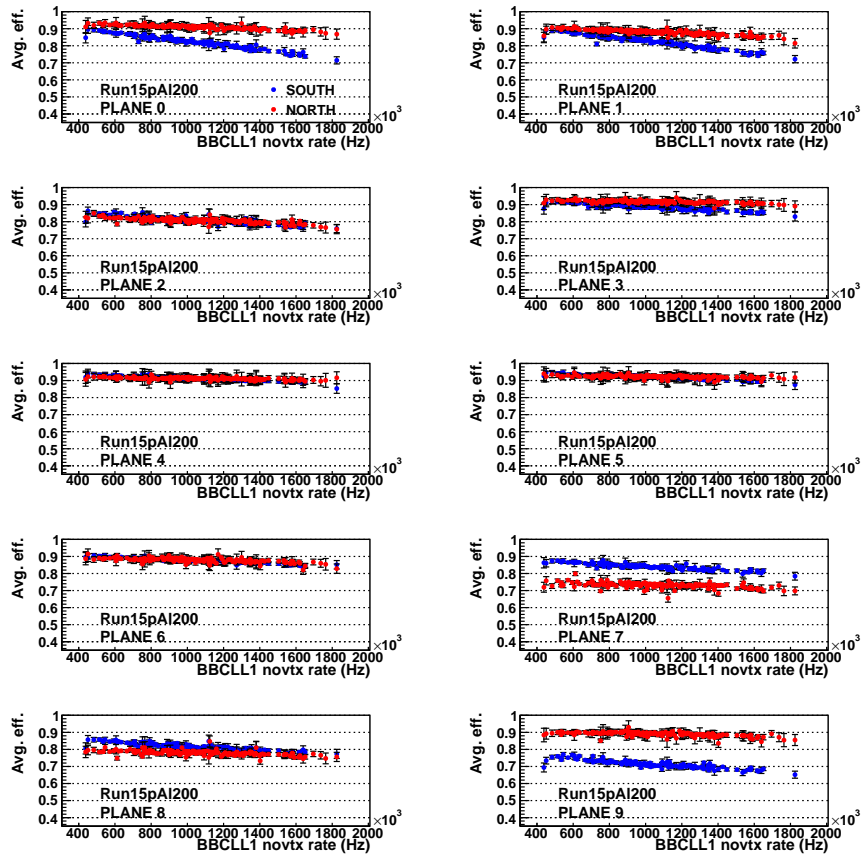


Figure 14: Average MuID tube efficiency of each plane as a function of BBCLL1 novortex trigger rate with MB triggered events in Run-15  $p+Al$ .

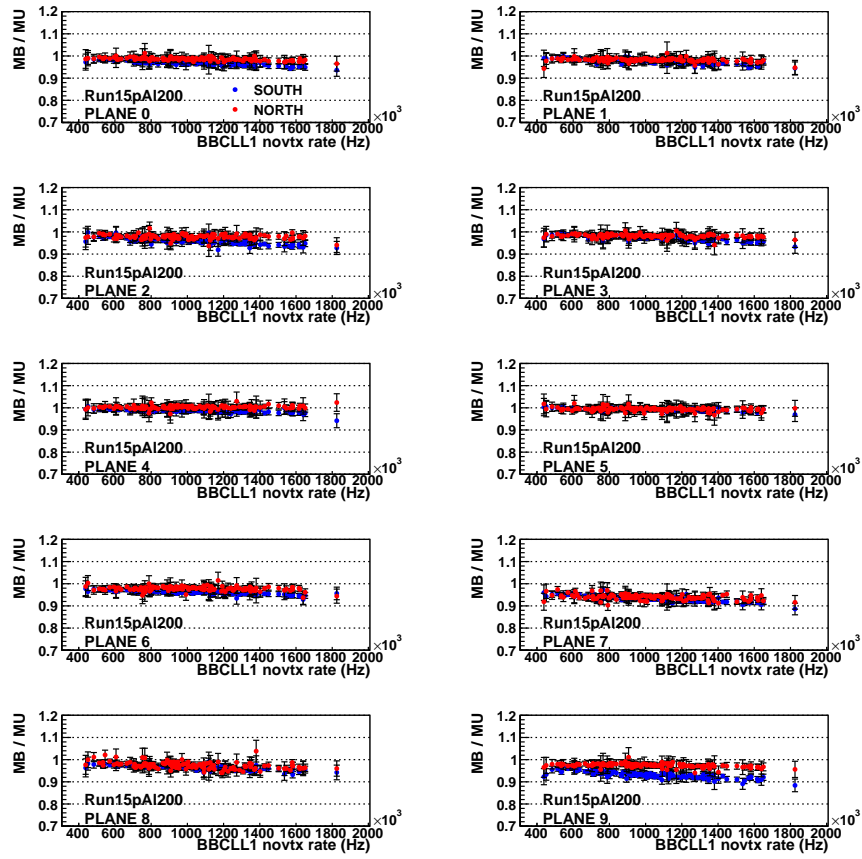


Figure 15: Comparison of average MuID tube efficiency of each plane as a function of BBCLL1 novertex trigger rate in Run-15  $p+Al$ .

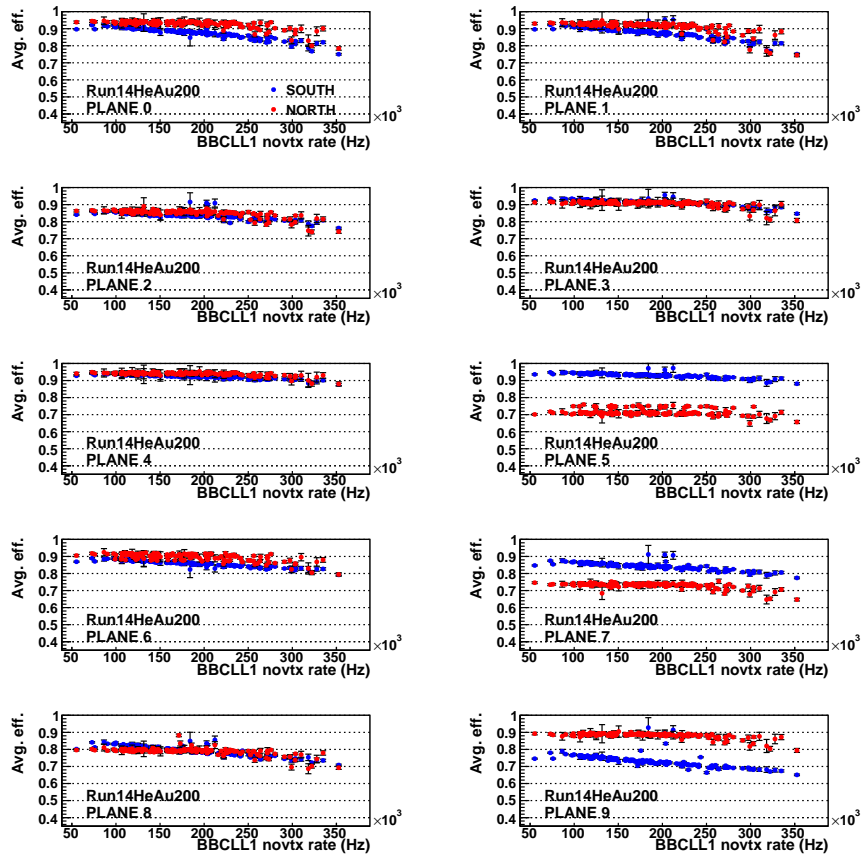


Figure 16: Average MuID tube efficiency of each plane as a function of BBCLL1 novortex trigger rate with MB triggered events in Run-14  $^3\text{He}+\text{Au}$ .

Another update on the MuID tube efficiency evaluation is to obtain channel-by-channel tube efficiency. The default method is to evaluate the MuID tube efficiency for each HV group and apply the same efficiency value to multiple channels inside the HV group. This approach is based on the assumption that the MuID tube efficiency is determined by biased HV. However, several recent studies show a discrepancy between the HV group method and the data driven method, and this may be due to different response of efficiency versus HV. In addition, the response of channels in a certain HV group may not be identical. Another advantage on evaluating the MuID tube efficiency in each HV group is to have more MuID track samples. In order to have more precise efficiency as a function of  $\varphi$  and  $\eta$ , the MuID tube efficiency has been calculated in each channel when a certain channel having enough MuID tracks. In not, the tube efficiency in a HV group is used. Fig. 17 show the MuID-2D trigger efficiency from the trigger emulator with the MuID tube efficiency in each HV group (red) and each channel (black). There is a small difference between two sets particularly in  $2.0 < |y| < 2.2$  at the south arm. Although it is about 10% relative effect, but it is good to have a correct rapidity shape. One thing to add is that several dead tubes are found which are not correctly implemented in the current simulation framework.

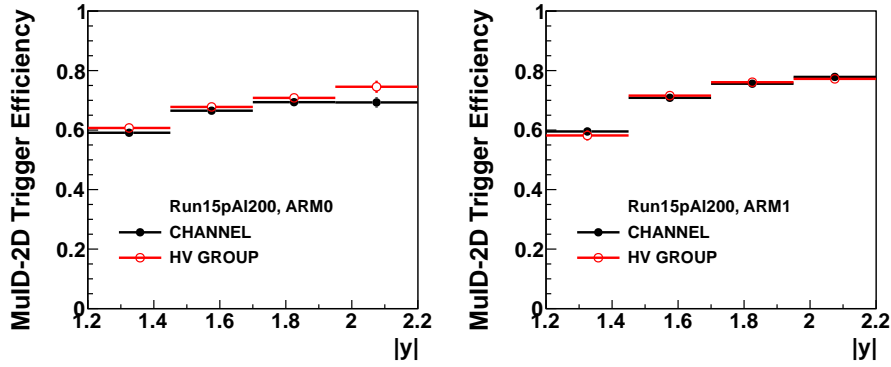


Figure 17: Comparison of the MuID-2D trigger efficiency from the trigger emulator with MuID tube efficiency evaluated in each HV group (red) and each channel (black) for Run-15  $p+Al$ .

### 3.2 Comparison of MuID-1D trigger efficiency

One way to verify rate-dependent MuID efficiency can be reproduced by simulation is to compare MuID-1D trigger efficiency between data and simulation. This is assumed by MuID trigger efficiency from the trigger emulation is agreed with that in the data which can be checked in the north arm where showing stable MuID performance. MuID efficiency files of 3 or 4 groups of runs for each data set are produced and used in single muon simulation to get rate-dependent MuID-1D trigger efficiency. In case of data, non-muon triggered events are used to evaluate the MuID-1D trigger efficiency. Figures 19, 20, and 21 show the comparison results between peripheral data and simulation, and simulation can reproduce the data quite nicely.

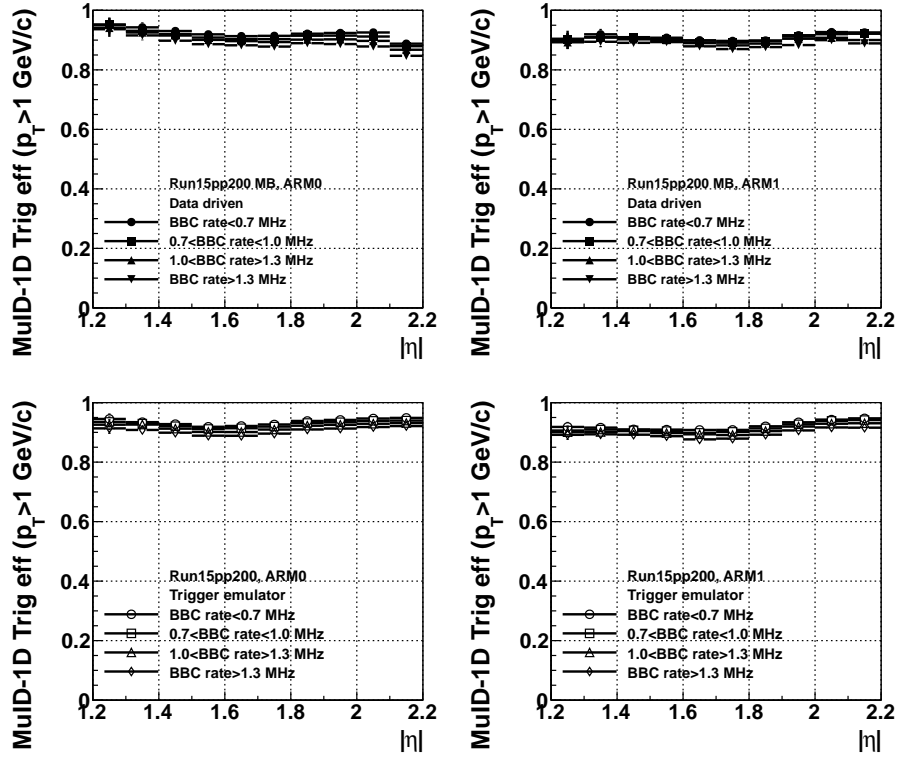


Figure 18: Comparison of the MuID-1D trigger efficiency as a function of  $\eta$  in three groups of runs in different BBCLL1 rate in Run-15  $^3\text{He}+\text{Au}$ .

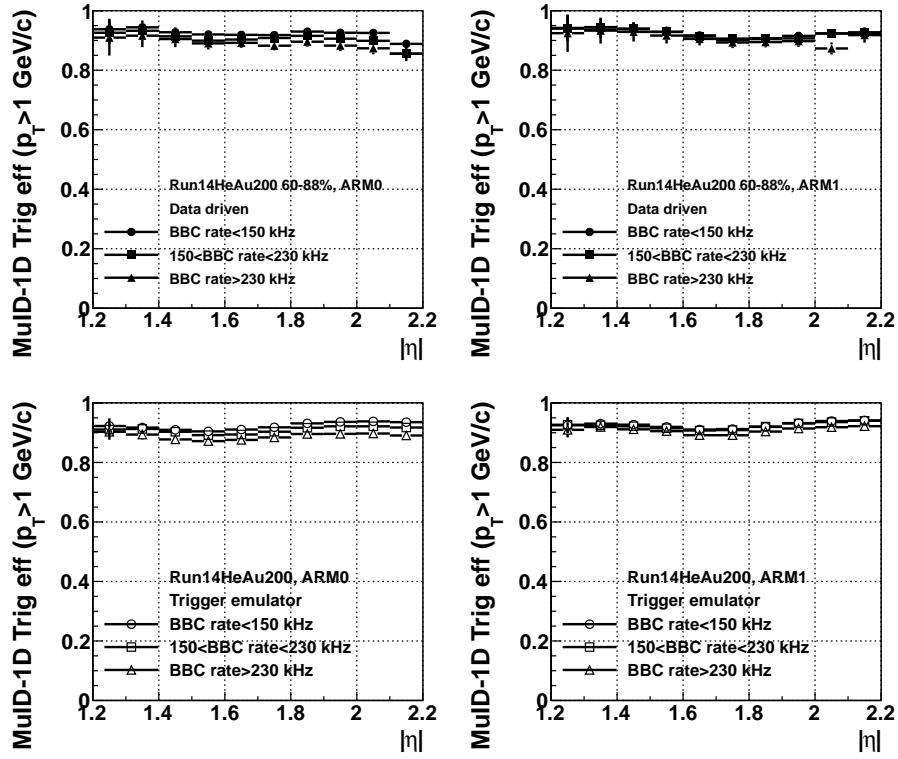


Figure 19: Comparison of the MuID-1D trigger efficiency as a function of  $\eta$  in three groups of runs in different BBCLL1 rate in Run-14  $^3\text{He}+\text{Au}$ .

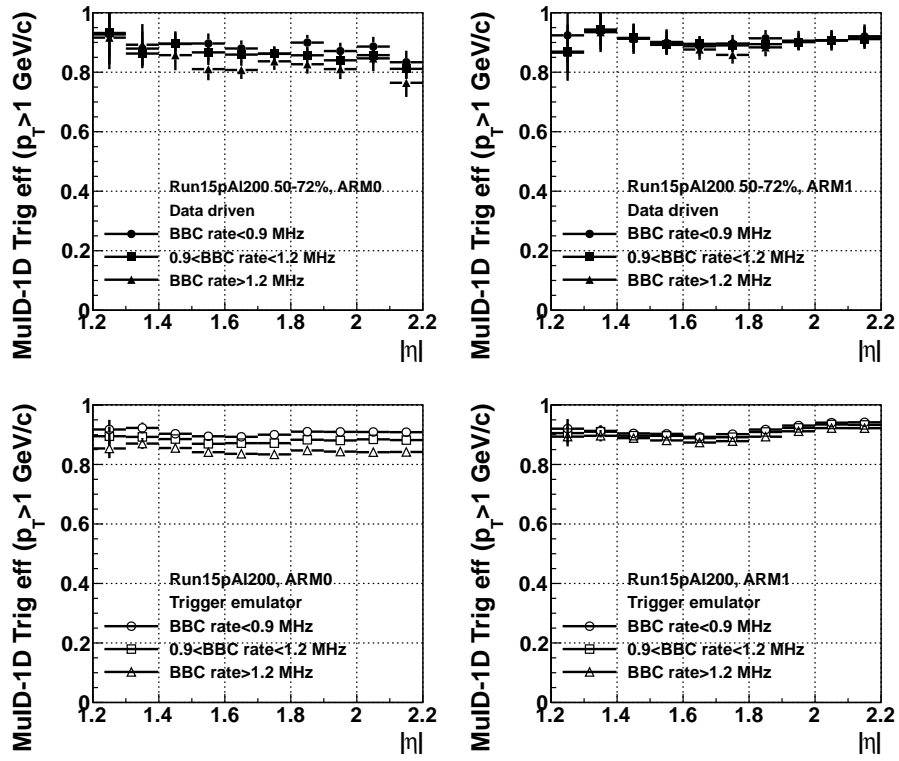


Figure 20: Comparison of the MuID-1D trigger efficiency as a function of  $\eta$  in three groups of runs in different BBCLL1 rate in Run-15  $p$ +Al.

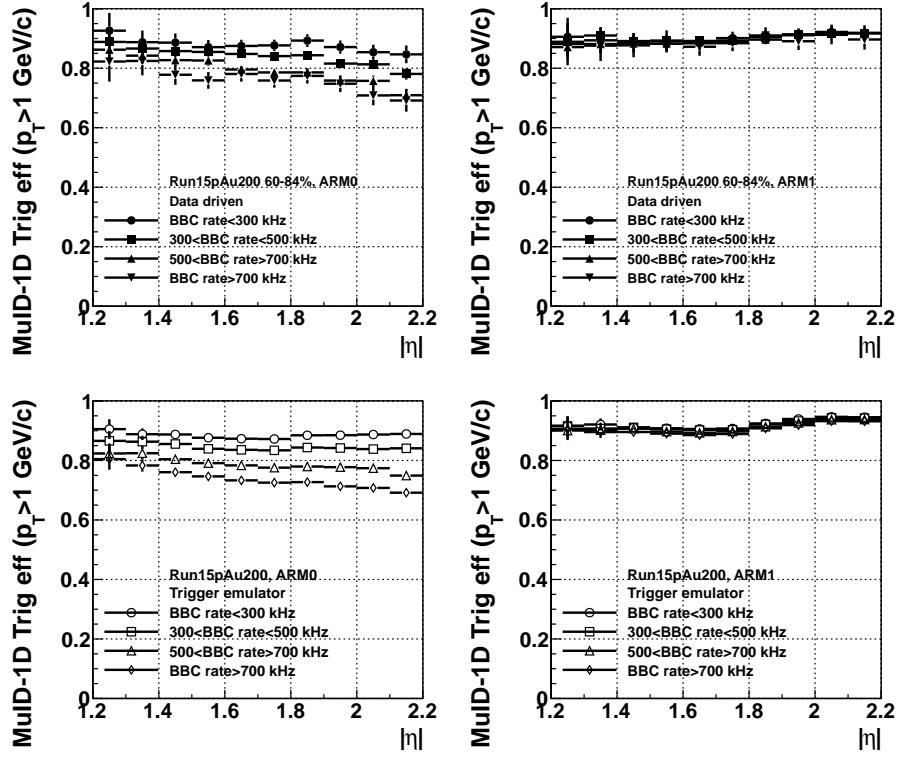


Figure 21: Comparison of the MuID-1D trigger efficiency as a function of  $\eta$  in three groups of runs in different BBCLL1 rate in Run-14  $p$ +Au.

### 3.3 MuTr efficiency

In the default simulation framework, the MuTr hit efficiency in each cathode plane is set to 98%. Top panels in Fig. 22 show a comparison of MuTr hit efficiency in each cathode plane with data and simulation. This efficiency also include a effect from dead area which can drop the efficiency. In order to have a correct comparison, a set of fiducial cut is applied to match active area in the MuTr between data and simulation. The default MuTr simulation agrees with data in the south arm, but it shows a higher efficiency at the north arm. The MuTr hit efficiency in each plane has been tuned to match the efficiency seen in data, and bottom panel of Fig. 22 shows a comparison with the tuning of MuTr hit efficiency.

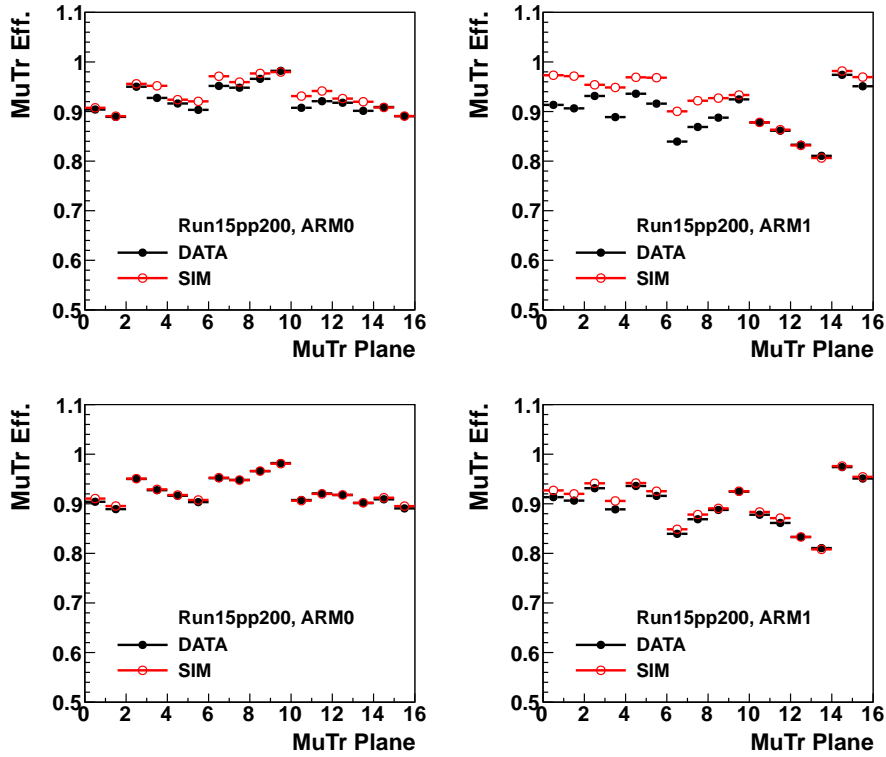


Figure 22: Comparison of MuTr hit efficiency between simulation and data in Run-15  $p+p$  before (top) and after (bottom) tuning.

After having the first preliminary results for QM18, 2-3% additional tuning is applied particularly for the north MuTr to further improve the matching of hit efficiency. Figure 23 shows a comparison of the updated MuTr hit efficiency between simulation and data.

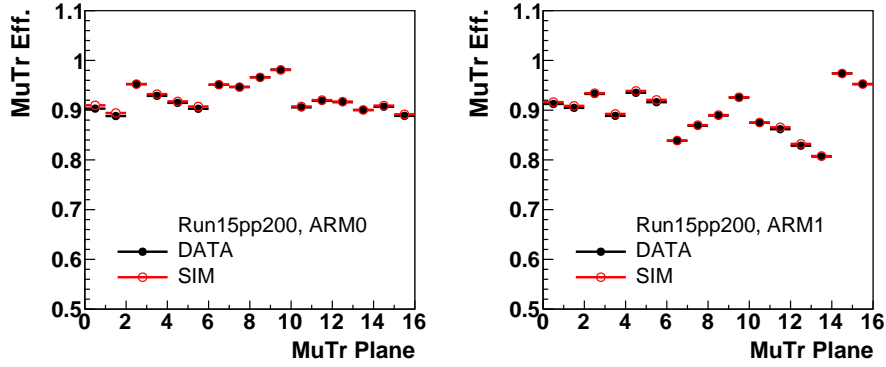


Figure 23: Comparison of MuTr hit efficiency between simulation and data in Run-15  $p+p$  with the additional tune.

### 3.4 Simulation procedure

The MuID-2D trigger efficiency and reconstruction efficiency has been evaluated with the default PHENIX simulation framework with GEANT4. One reference run for each data set (416201 for Run-14  $^3\text{He}+\text{Au}$ , 431846 for Run-15  $p+p$ , 437940 for Run-15  $p+\text{Al}$ , and 434153 for Run-15  $p+\text{Au}$ ) is used for embedding simulation. The simulation procedure is described below.

- Generate PYTHIA8  $J/\psi \rightarrow \mu\mu$  event at vertex position from the background DST
- Run GEANT4 simulation
- Reconstruction with the background DST including realistic dead map in the MuTr and tube efficiency in the MuID

For systematic study due to initial  $p_T$  and  $\eta$  shapes, weighting factors to PYTHIA8 based on the previous measurements in  $p+p$  and  $d+\text{Au}$  at  $\sqrt{s_{NN}} = 200$  GeV are used to check their effect as shown in Fig. 24.

### 3.5 BBCLL1 rate dependent efficiency correction

The MuID tube efficiency in all data sets shown in Fig. 11, 14, and 16 show a dependence on BBCLL1 rate, although the magnitude of efficiency drop is different among data sets. In order to make sure the actual efficiency variation of raw yield of dimuons is fully corrected by simulation with the MuID tube efficiency, Independent analyses in two bins of high and low BBCLL1 rate has been done. Two sets of simulation with corresponding MuID tube efficiency are used to evaluate MuID-2D trigger efficiency and reconstruction efficiency.

Figure 27 shows the MuID-2D trigger efficiency (top) and reconstruction efficiency (bottom) as a function of rapidity for three sets of MuID tube efficiency,

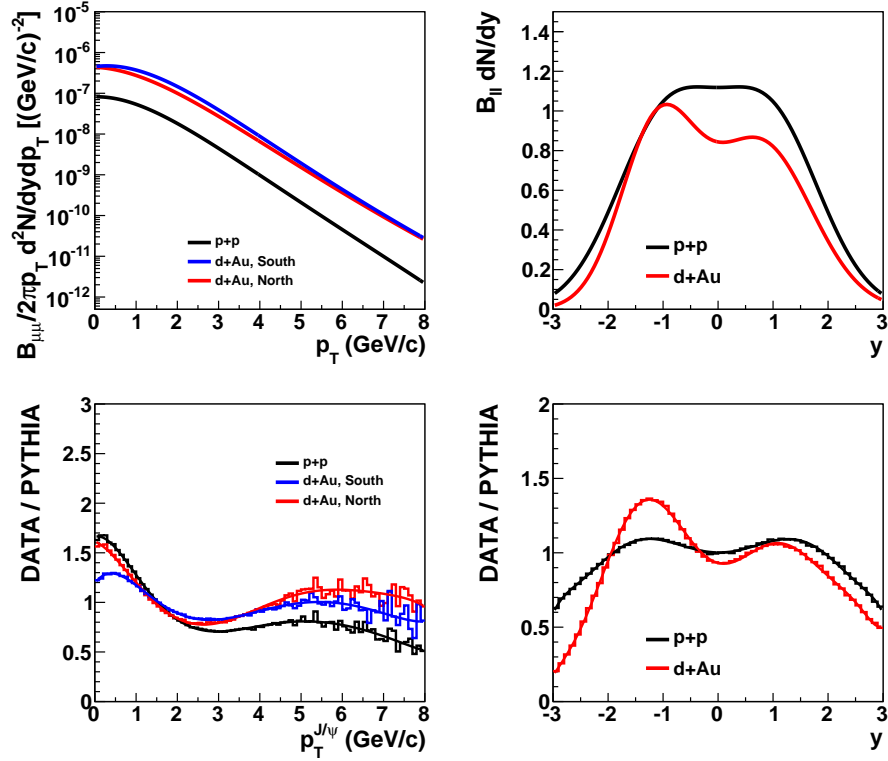


Figure 24: Fit functions to the previous measurements (top) and ratio to PYTHIA8 (bottom).

low (BBC rate < 150 kHz), high (BBC rate > 150 kHz) BBCLL1 rate, and combined runs in Run-14  $^3\text{He}+\text{Au}$  data. Fig. 28 the ratio of  $J/\psi$  yield in low (red) or high (blue) BBCLL1 runs to  $J/\psi$  yield in combined runs without (top) and with (bottom) corrections. In case of Run-14  $^3\text{He}+\text{Au}$ , the difference between low and high BBCLL1 rate runs is small as shown in the top panel. Fig. 29 shows efficiencies in low (BBC rate < 1 MHz), high (BBC rate > 1 MHz) BBCLL1 rate, and combined runs in Run-15  $p+\text{Al}$  data. In case of Run-15  $p+\text{Al}$ , the difference of efficiencies between low and high rate runs is larger than that in Run-14  $^3\text{He}+\text{Au}$ , and the variation of  $J/\psi$  yield from the yield in combined runs is  $\sim 10 - 20\%$  at the south arm as shown in the top panel of Fig. 30. After correction, they are agreed within statistical uncertainties as shown in the bottom panel. Figures 31 and 32 show same plots for Run-15  $p+\text{Au}$ . Although the BBCLL1 trigger rate in the  $p+\text{Au}$  run is lower than that in the  $p+\text{Al}$  run, but the raw yield variation at the south arm is much larger. After correction shown in the bottom panel of Fig. 32, raw yields of  $J/\psi$  in high (BBC rate > 550 kHz) and low (BBC rate < 550 kHz) BBCLL1 rate runs are agreed.

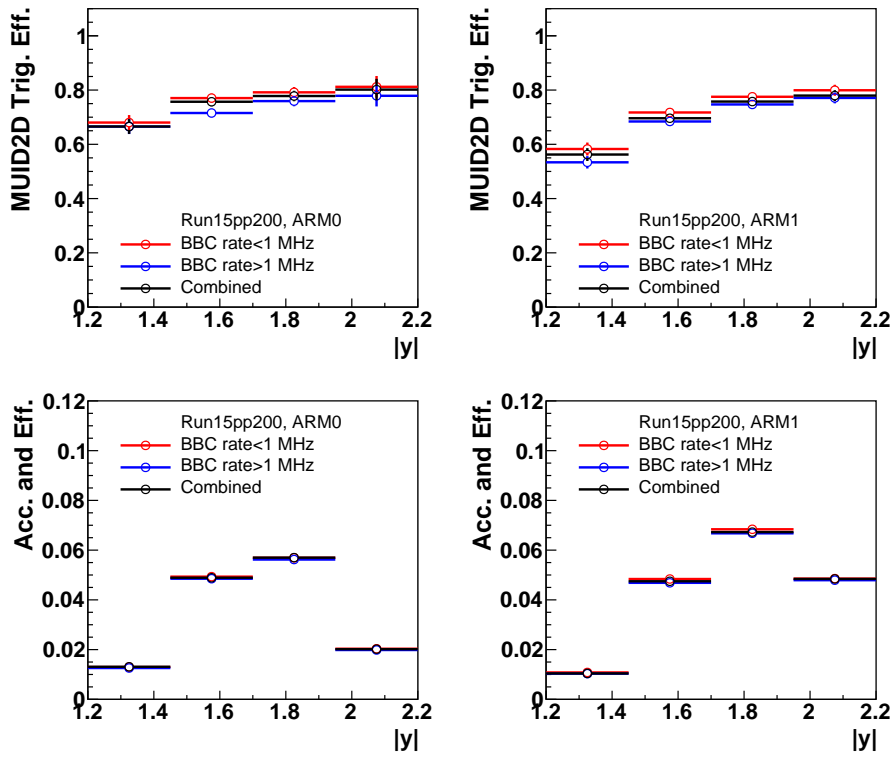


Figure 25: MuID-2D trigger efficiency (top) and reconstruction efficiency (bottom) of  $J/\psi \rightarrow \mu\mu$  as a function of rapidity in runs of low, high, and combined BBCLL1 novertex rate of Run-15  $p+p$ .

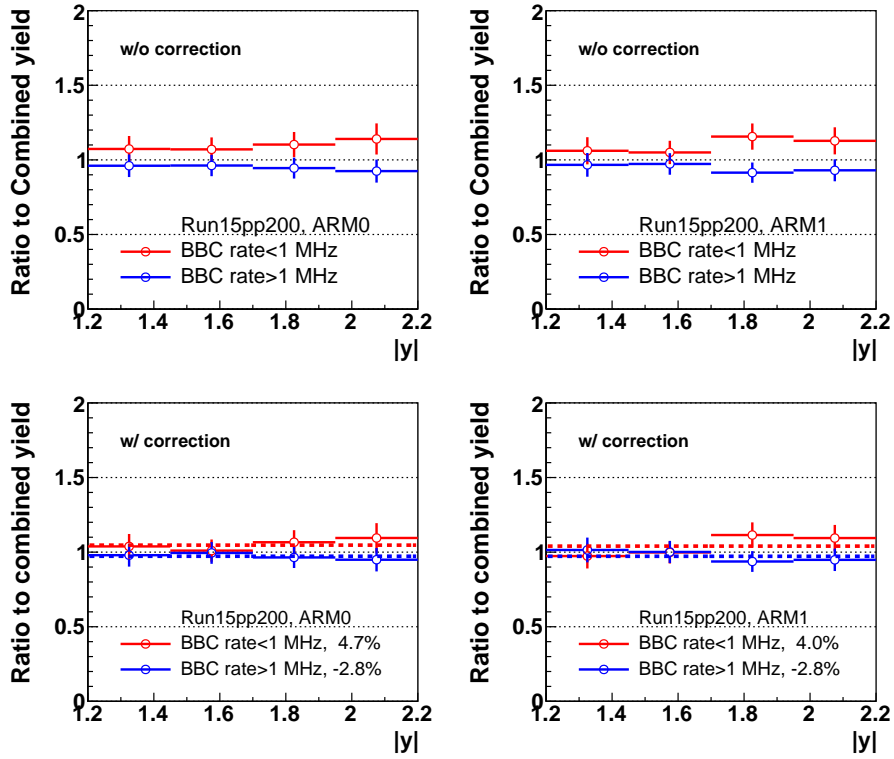


Figure 26: Yield ratio of low or high BBCLL1 novertex rate runs to combined runs as a function of rapidity without (top) and with (bottom) corrections in Run-15  $p+p$ .

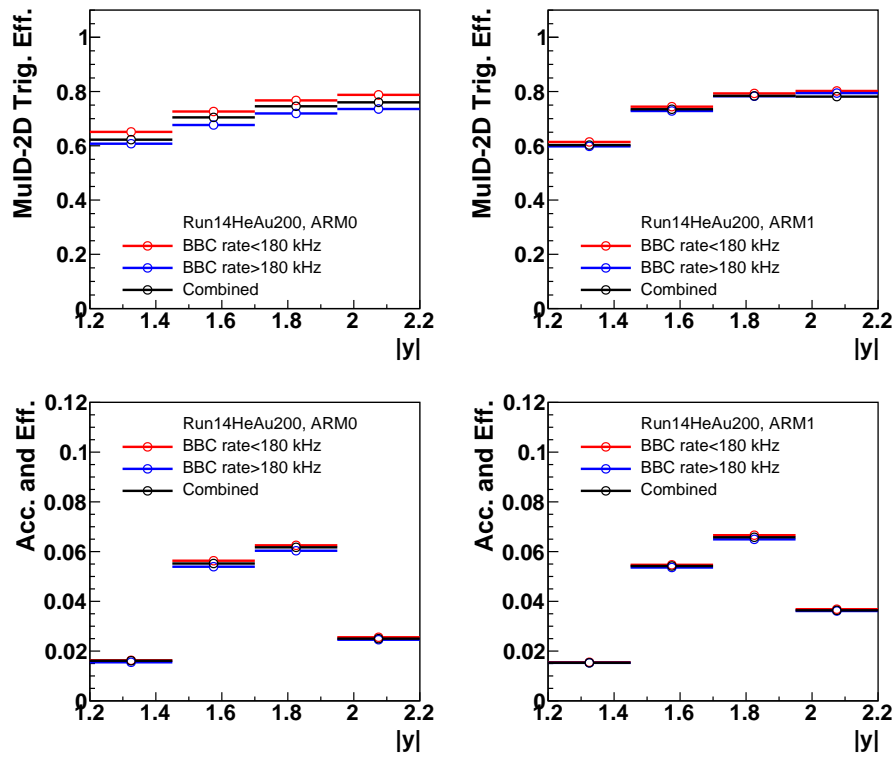


Figure 27: MuID-2D trigger efficiency (top) and reconstruction efficiency (bottom) of  $J/\psi \rightarrow \mu\mu$  as a function of rapidity in runs of low, high, and combined BBCLL1 novertex rate of Run-14  $^3\text{He}+\text{Au}$ .

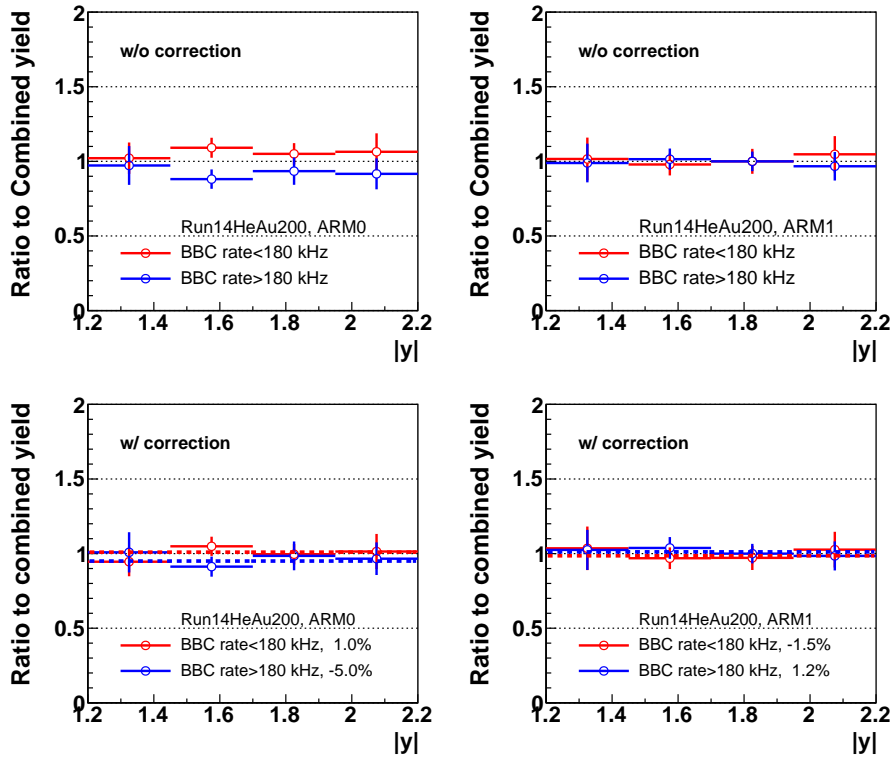


Figure 28: Yield ratio of low or high BBCLL1 novertex rate runs to combined runs as a function of rapidity without (top) and with (bottom) corrections in Run-14  $^3\text{He}+\text{Au}$ .

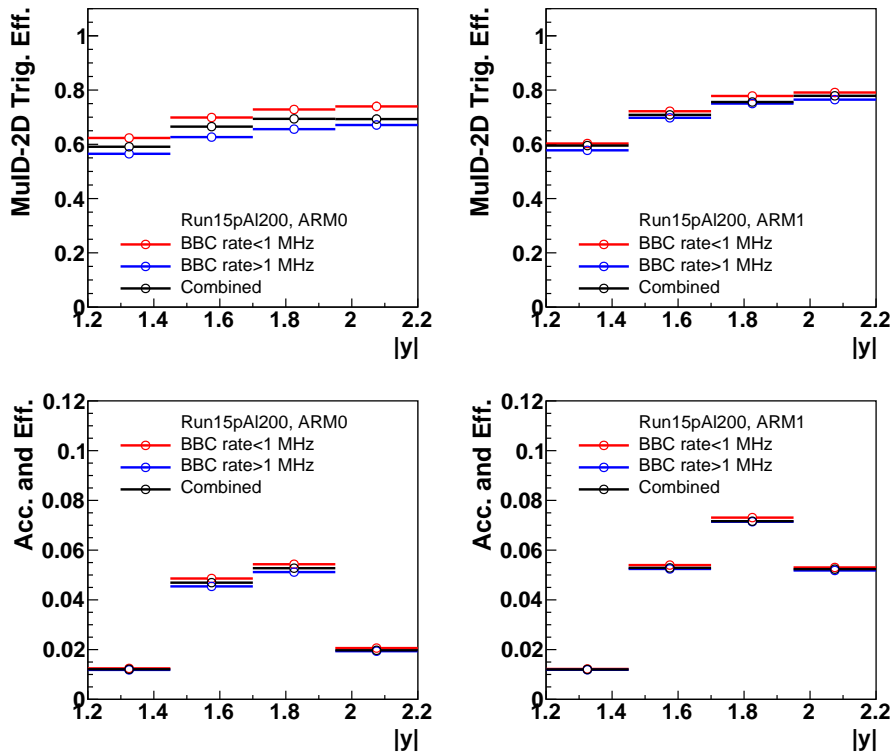


Figure 29: MuID-2D trigger efficiency (top) and reconstruction efficiency (bottom) of  $J/\psi \rightarrow \mu\mu$  as a function of rapidity in runs of low, high, and combined BBCLL1 novertex rate of Run-15  $p$ +Al.

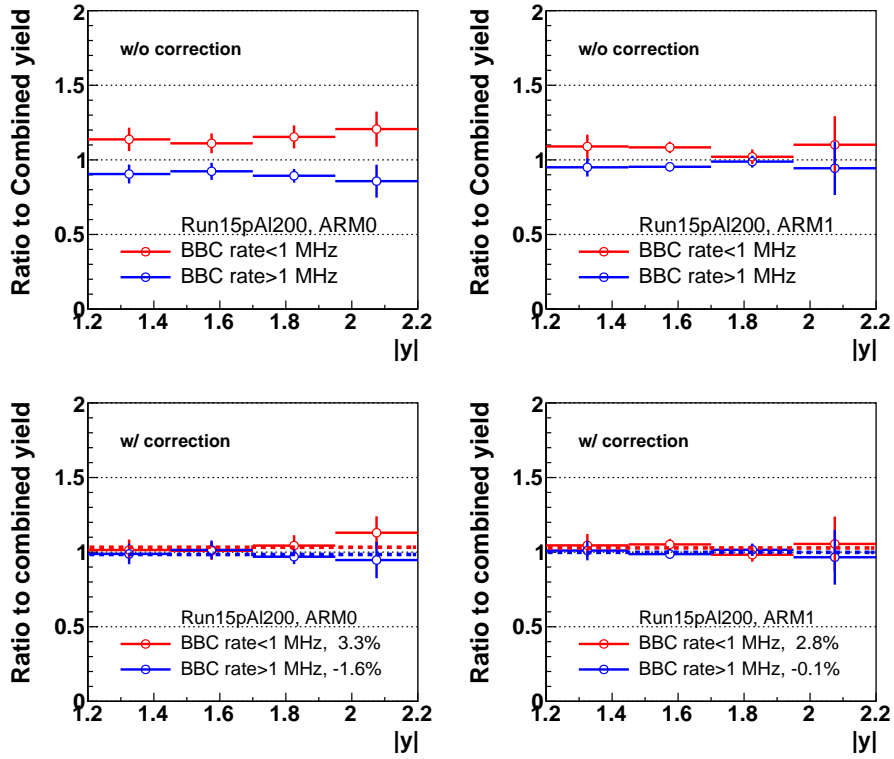


Figure 30: Yield ratio of low or high BBCLL1 novertex rate runs to combined runs as a function of rapidity without (top) and with (bottom) corrections in Run-15  $p+Al$ .

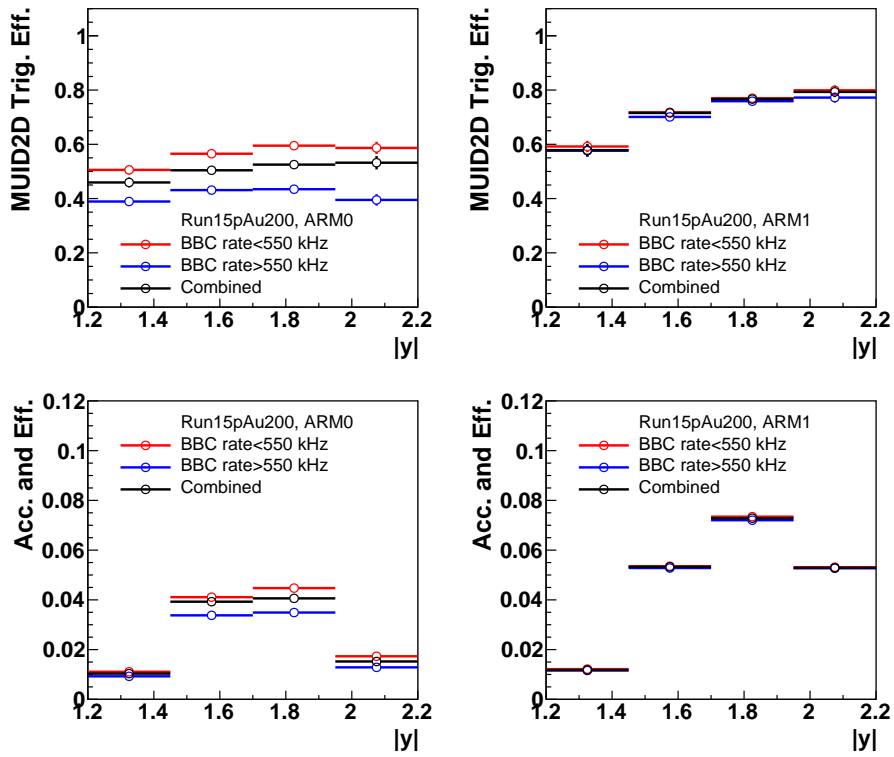


Figure 31: MuID-2D trigger efficiency (top) and reconstruction efficiency (bottom) of  $J/\psi \rightarrow \mu\mu$  as a function of rapidity in runs of low, high, and combined BBCLL1 novertex rate of Run-15  $p$ +Au.

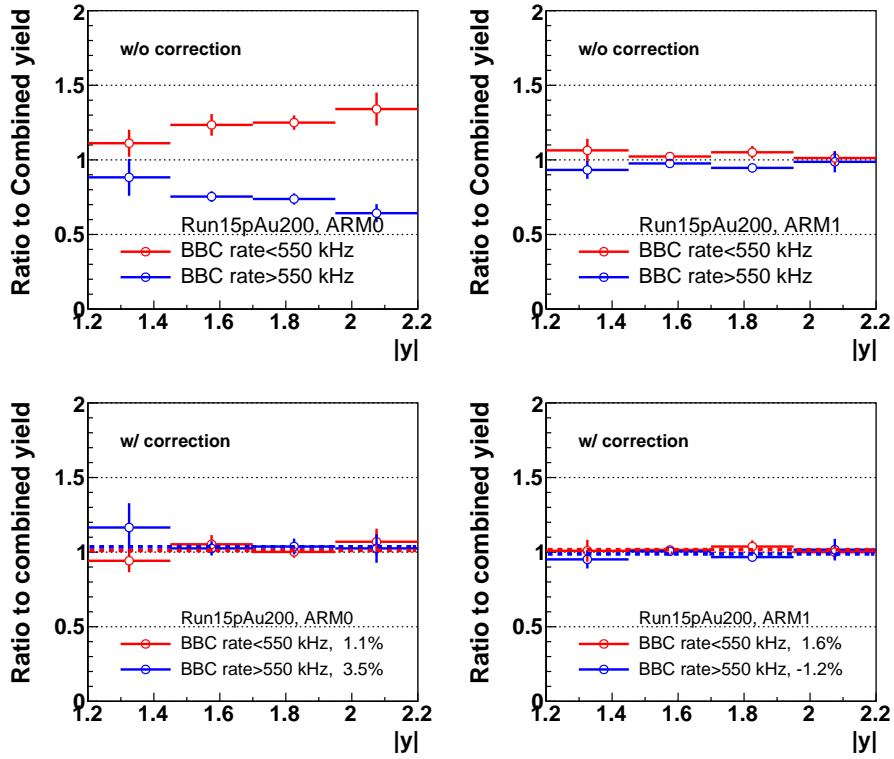


Figure 32: Yield ratio of low or high BBCLL1 novertex rate runs to combined runs as a function of rapidity without (top) and with (bottom) corrections in Run-15  $p+Au$ .

### 3.6 MuID-2D trigger efficiency

The MuID-2D trigger efficiency has been evaluated with the trigger emulator, because the number of  $J/\psi$  candidates in MB data sets is quite small. One thing noticed when comparing with the MuID-2D trigger efficiency from the data driven method and the trigger emulator, there is a multiplicity effect which cause a higher trigger efficiency. Left panels of Figs 35 and 36 show the MuID-2D trigger efficiency at the south arm (Au-going direction) where track multiplicity is higher than that at the north arm, the trigger efficiency from the data driven method (solid blue points) is higher than the trigger efficiency in non-embedding simulation (open black points) which only including  $J/\psi$  hard scattering event from PYTHIA8. In order to reproduce the multiplicity effect seen in the data, the number of MuID track is checked in data events including  $J/\psi$  candidate. When preparing background DST for embedding, the ratio of event including additional MuID tracks obtained from the data is used to filter background events for embedding. The trigger efficiency from embedding simulation with the filtered background DST can reproduce the multiplicity effect in the MuID-2D trigger efficiency. A systematic study has been done to take into account  $\sim 5\%$  difference in the MuID-1D trigger efficiency between data and trigger emulator as shown in the middle panels of Figs. 33, 45, 46, and 47. The MuID-2D trigger efficiency with the additional correction is shown in the bottom panels.

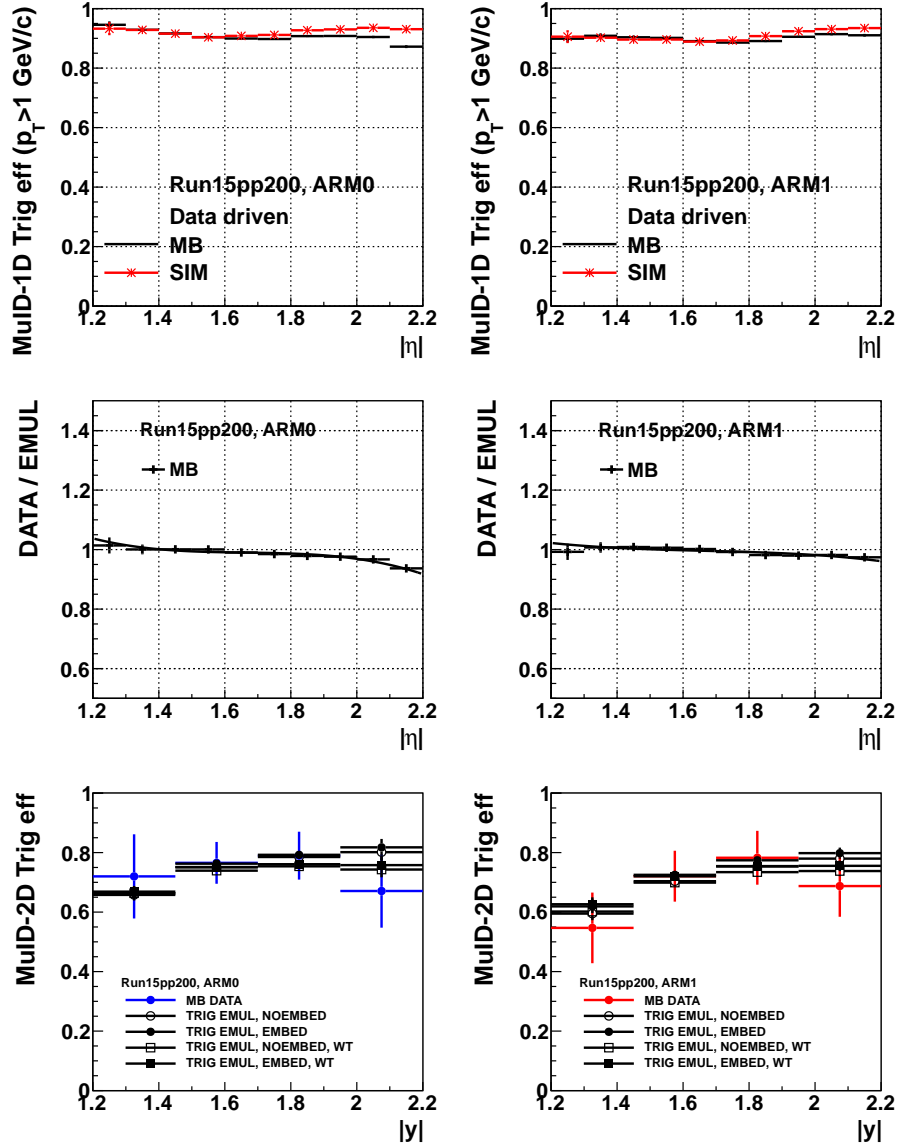


Figure 33: MuID-2D trigger efficiency as a function of rapidity in Run-15  $p+p$ . Comparison between data driven method and trigger emulator is also shown.

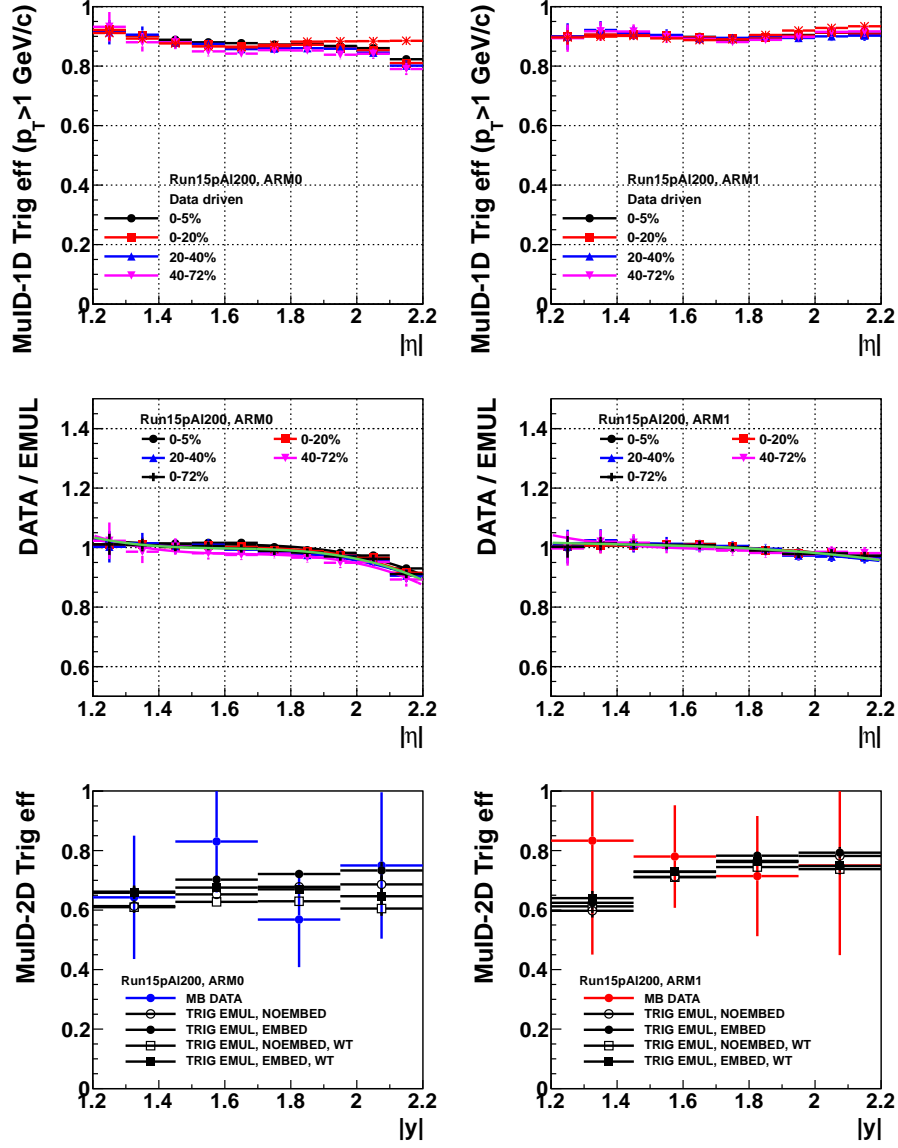


Figure 34: MuID-2D trigger efficiency as a function of rapidity in Run-15  $p$ +Al. Comparison between data driven method and trigger emulator is also shown.

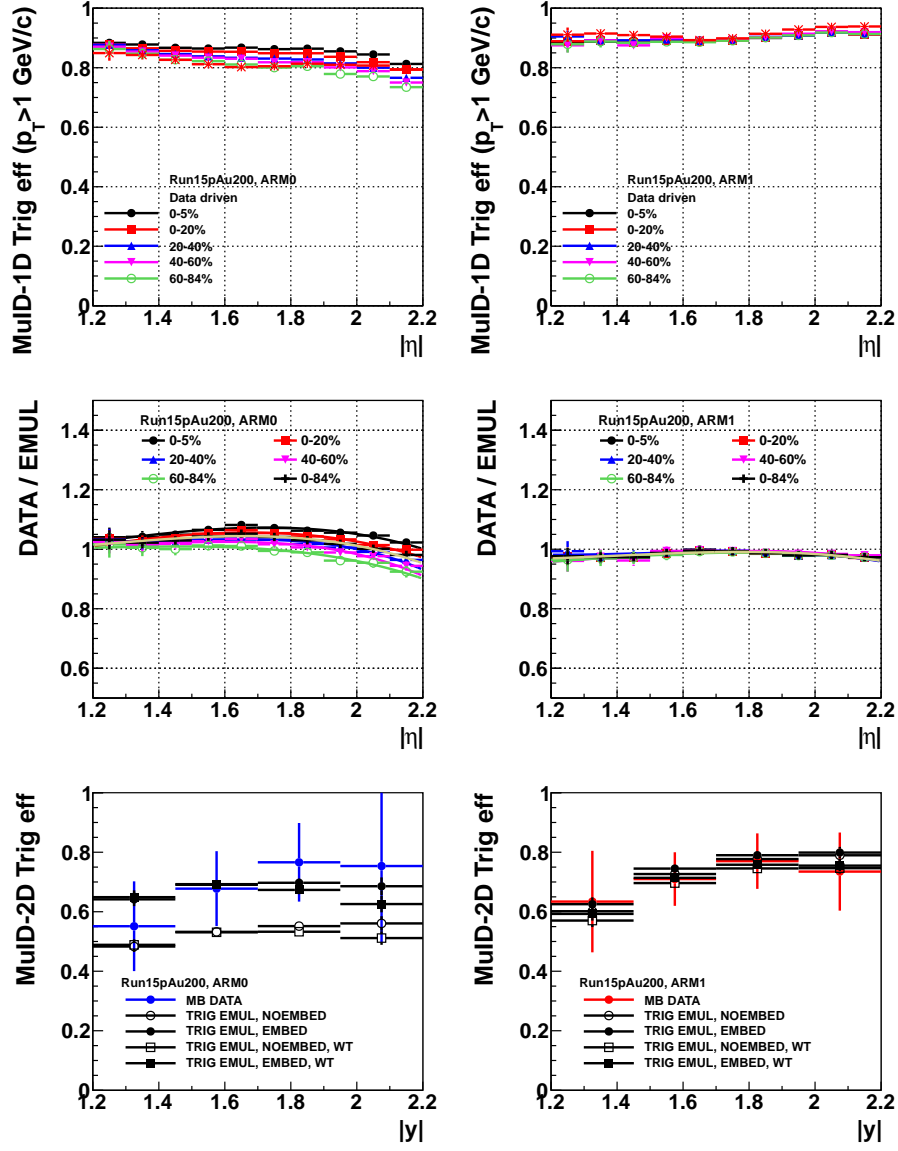


Figure 35: MuID-2D trigger efficiency as a function of rapidity in Run-15  $p$ +Au. Comparison between data driven method and trigger emulator is also shown.

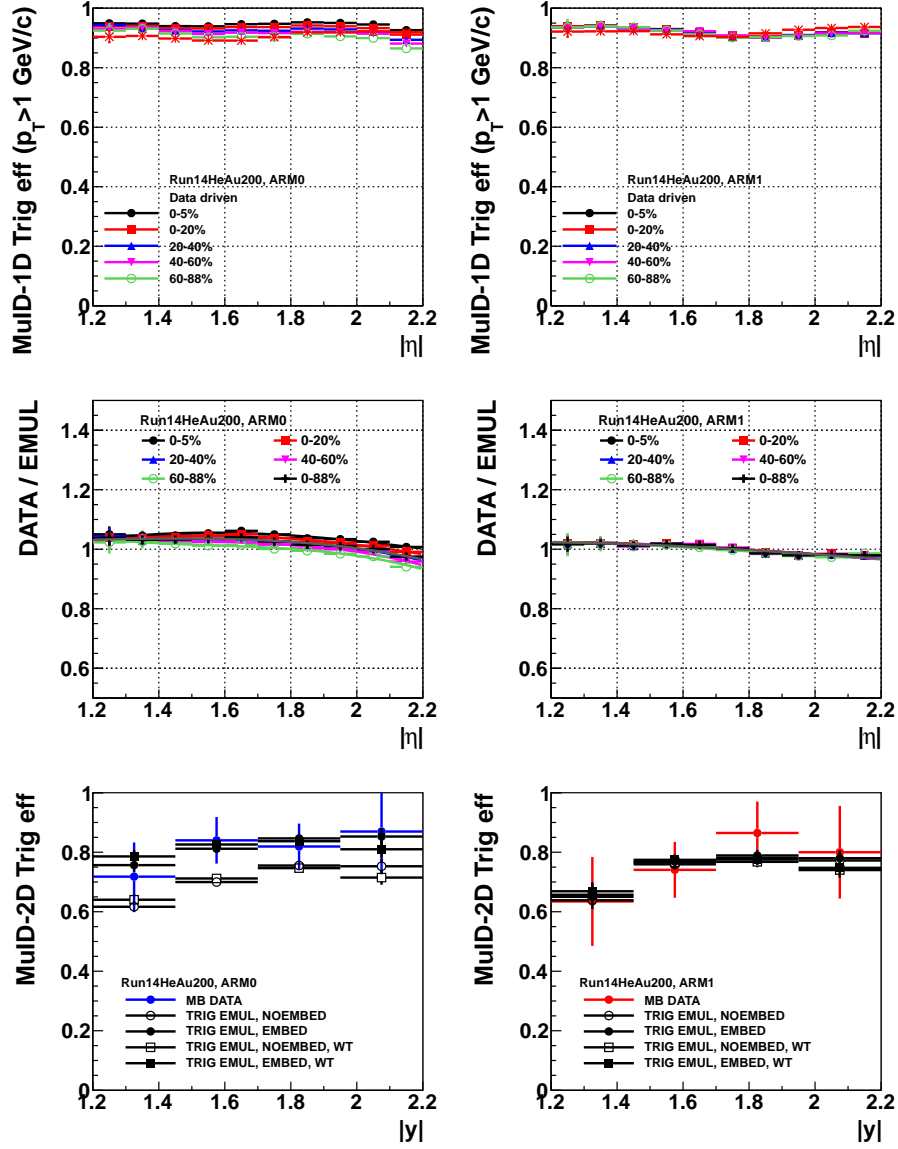


Figure 36: MuID-2D trigger efficiency as a function of rapidity in Run-14  $^3\text{He}+\text{Au}$ . Comparison between data driven method and trigger emulator is also shown.

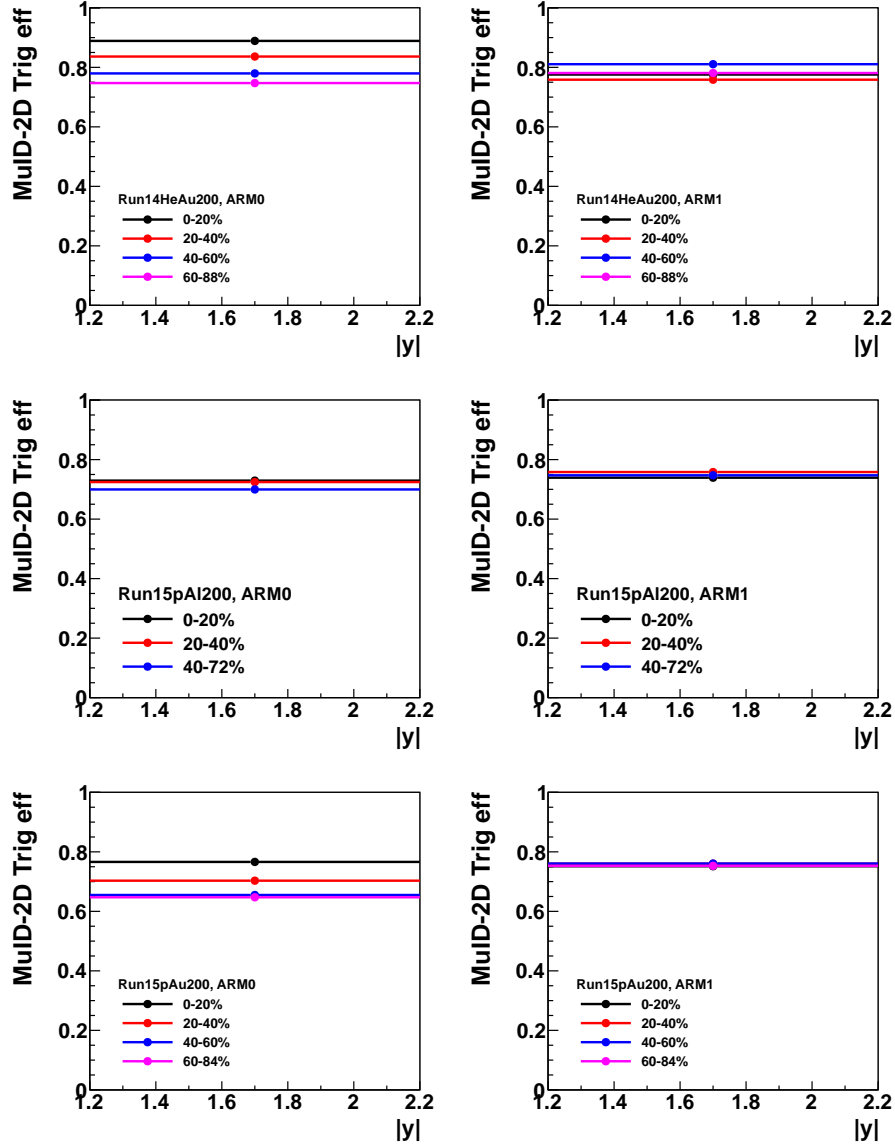


Figure 37: Centrality dependent MuID-2D trigger efficiency in the integrated rapidity in Run-14  $^3\text{He}+\text{Au}$  (top), Run-15  $p+\text{Al}$  (middle), and  $p+\text{Au}$  (bottom).

For the trigger efficiency as a function of  $p_T$ , fit functions to  $p_T$  spectra of all reconstructed  $J/\psi$  and reconstructed  $J/\psi$  passing the trigger emulator are used to obtain a smooth curve up to high  $p_T$  where a statistical fluctuation of simulation becomes large. Figure 38 shows an example of fit the  $p_T$  spectra with the modified Hagedorn function. In order to evaluate systematic uncertainty, the difference of MuID-1D trigger efficiency between data and simulation has been used shown in the top panel of Figs. 42, 39, 40, and 41 is used as a weight for single muons from  $J/\psi$ . The middle panels show the MuID-2D trigger efficiency as a function  $p_T$  with and without weighting. The fit function to the average value is used for trigger efficiency correction, and the difference between two cases of efficiency shown in the bottom panels is assigned to systematic uncertainty.

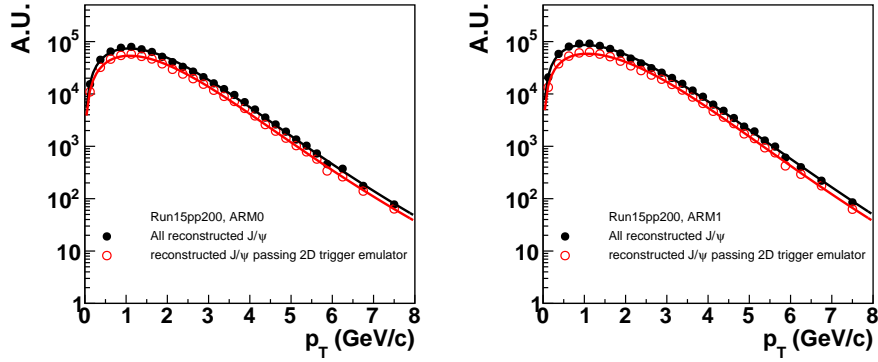


Figure 38:  $p_T$  spectra of all reconstructed  $J/\psi$  and reconstructed  $J/\psi$  passing the 2D trigger emulator in simulation for Run-15  $p+p$  and fit with the modified Hagedorn function.

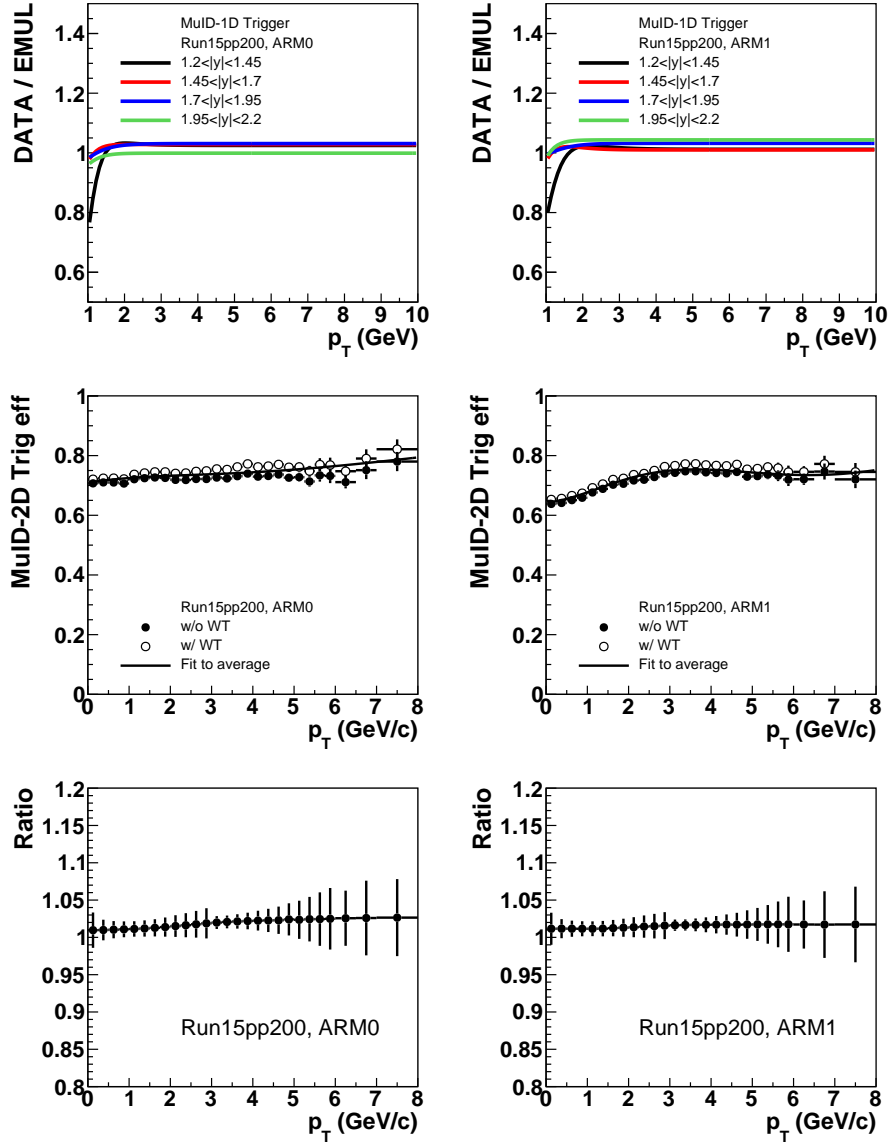


Figure 39: (Top) Comparison of the MuID-1D trigger efficiency as a function of  $p_T$  between data and trigger emulator. (Middle) The MuID-2D trigger efficiency as a function of  $p_T$  in Run-15  $p+p$ . (Bottom) Ratio between the combined efficiency shown as a fit function and the trigger efficiency without weighting for systematic uncertainty evaluation.

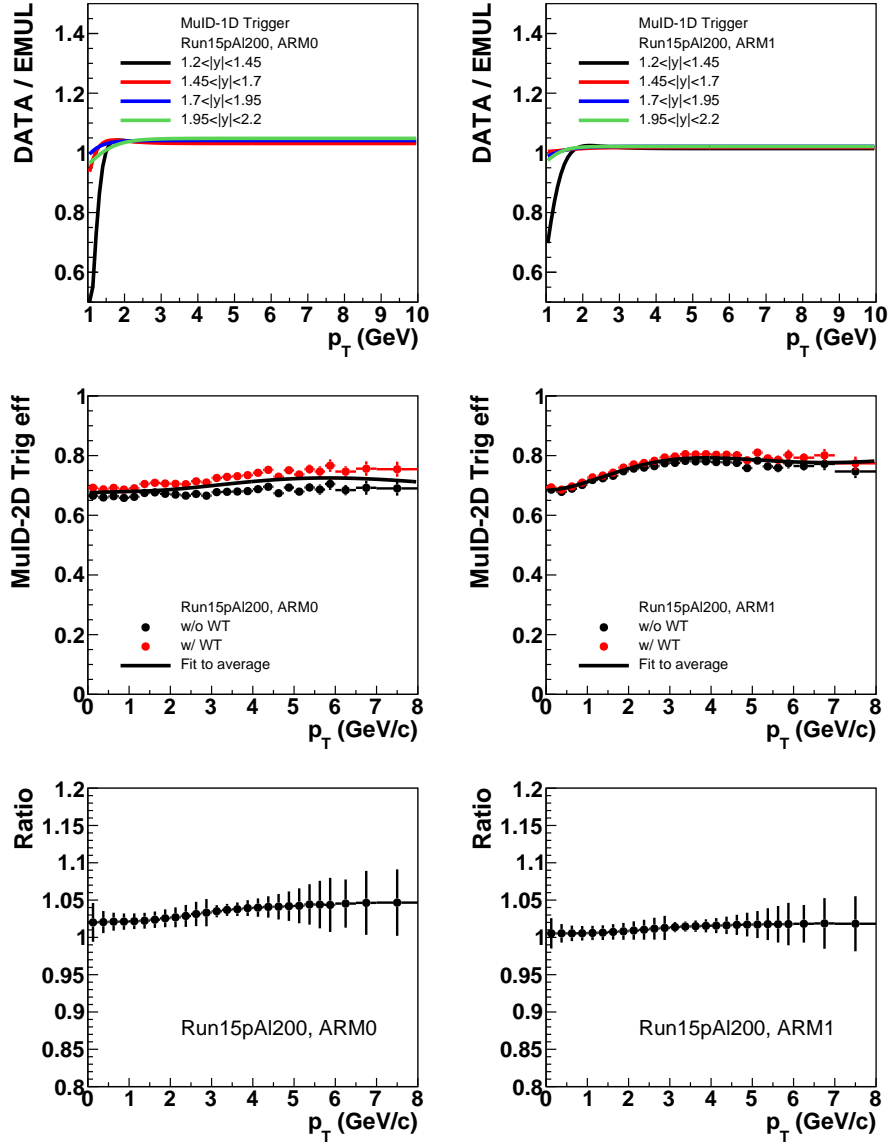


Figure 40: (Top) Comparison of the MuID-1D trigger efficiency as a function of  $p_T$  between data and trigger emulator. (Middle) The MuID-2D trigger efficiency as a function of  $p_T$  in Run-15  $p$ +Al. (Bottom) Ratio between the combined efficiency shown as a fit function and the trigger efficiency without weighting for systematic uncertainty evaluation.

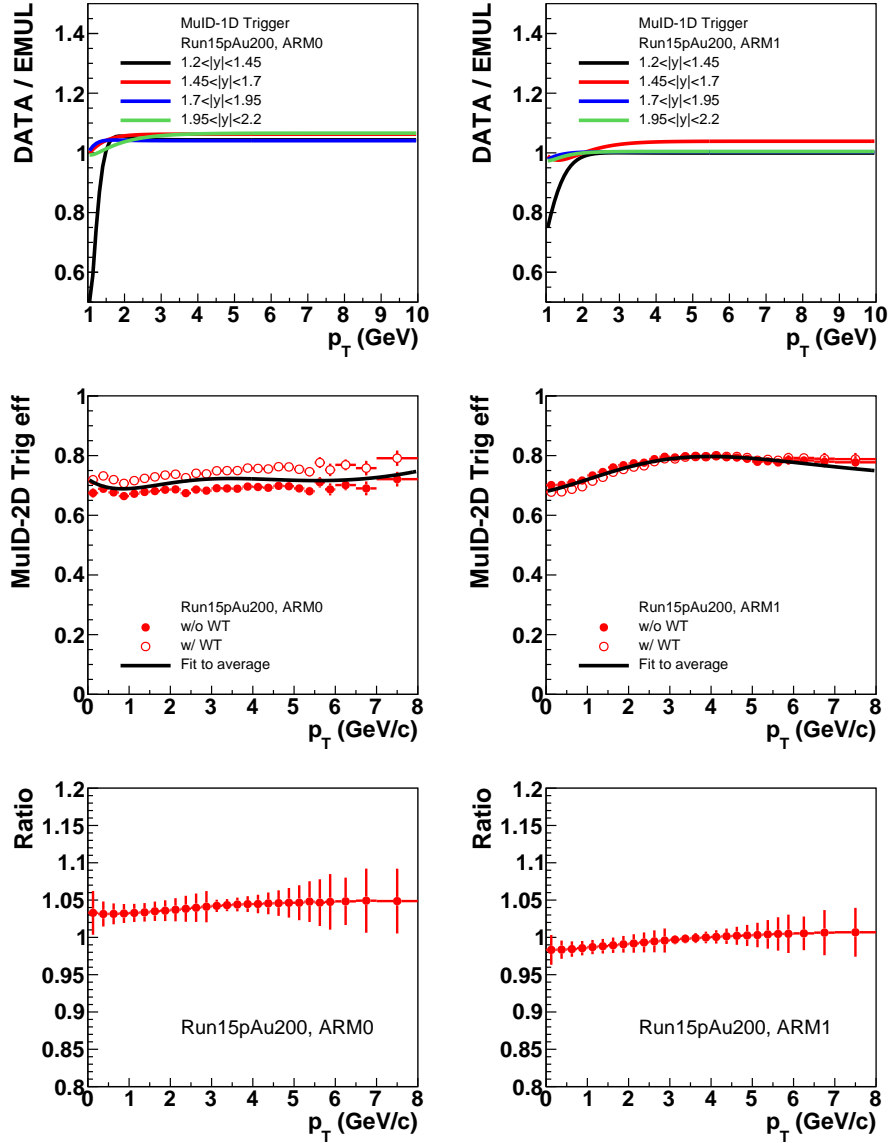


Figure 41: (Top) Comparison of the MuID-1D trigger efficiency as a function of  $p_T$  between data and trigger emulator. (Middle) The MuID-2D trigger efficiency as a function of  $p_T$  in Run-15  $p+Au$ . (Bottom) Ratio between the combined efficiency shown as a fit function and the trigger efficiency without weighting for systematic uncertainty evaluation.

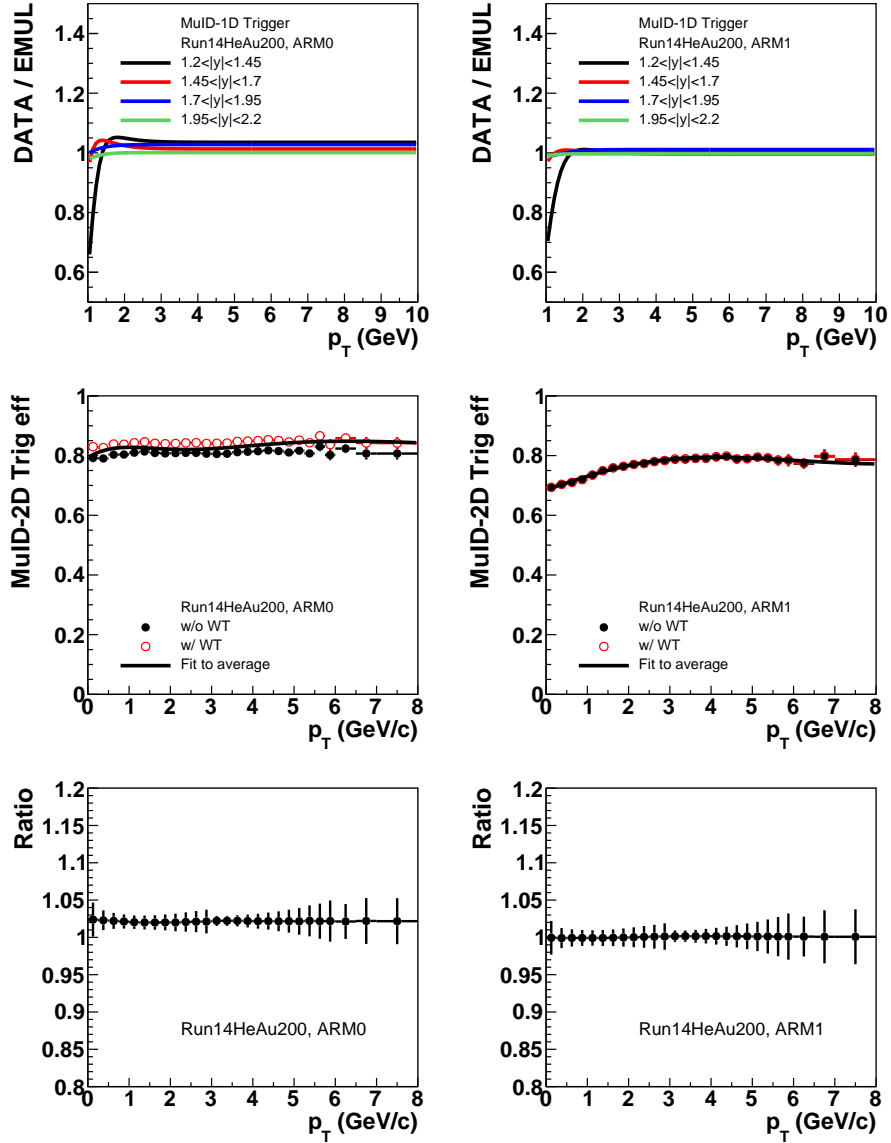


Figure 42: (Top) Comparison of the MuID-1D trigger efficiency as a function of  $p_T$  between data and trigger emulator. (Middle) The MuID-2D trigger efficiency as a function of  $p_T$  in Run-14  $^3\text{He}+\text{Au}$ . (Bottom) Ratio between the combined efficiency shown as a fit function and the trigger efficiency without weighting for systematic uncertainty evaluation.

### 3.7 Acceptance and reconstruction efficiency

Acceptance and reconstruction efficiency has been evaluated based on the procedure described in Sec. 3.4. In order to do a systematic study, initial  $p_T$  and  $y$  distributions of  $J/\psi$  have been modified based on measured  $p+p$  and  $d+Au$  data as shown in 24. Modification of  $p_T$  shape does not affect to the acceptance and reconstruction efficiency in the integrated  $p_T$ , and  $< 2\%$  variation is observed. For acceptance and reconstruction efficiency as a function of  $p_T$ , fit functions to generated and reconstructed  $p_T$  spectra shown in Fig. 43 are used to obtained a smooth acceptance and efficiency curve.

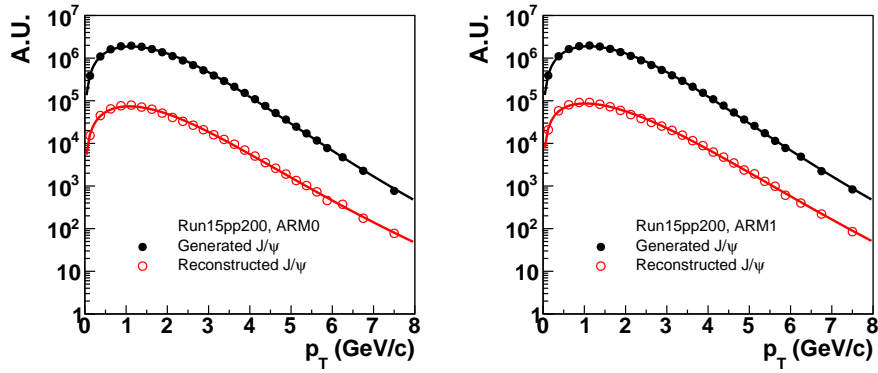


Figure 43:  $p_T$  spectra of generated reconstructed  $J/\psi$  and reconstructed  $J/\psi$  for Run-15  $p+p$  and fit with the modified Hagedorn function.

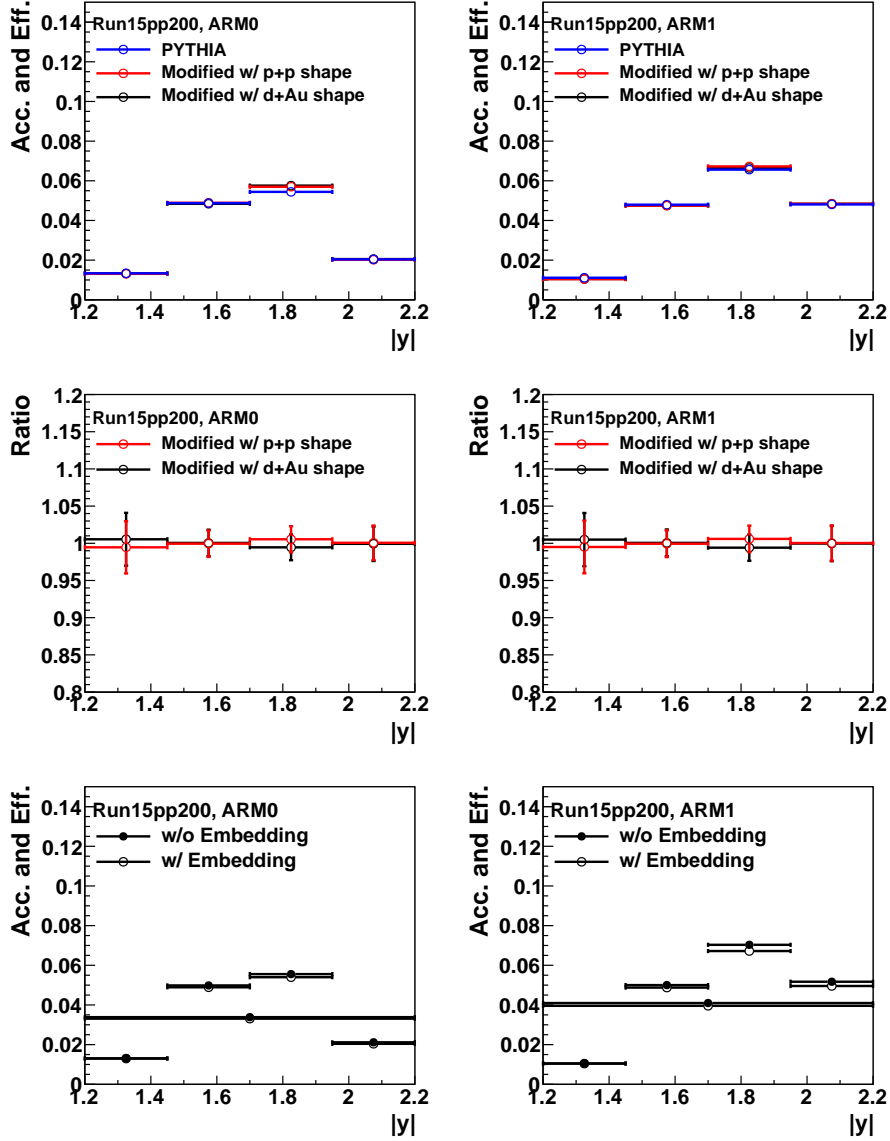


Figure 44: Acceptance and reconstruction efficiency of  $J/\psi$  as a function of rapidity in Run-15  $p+p$ . Comparisons between various initial  $p_T$  and  $y$  distributions (top and middle) as well as between embedding and non-embedding simulation are shown.

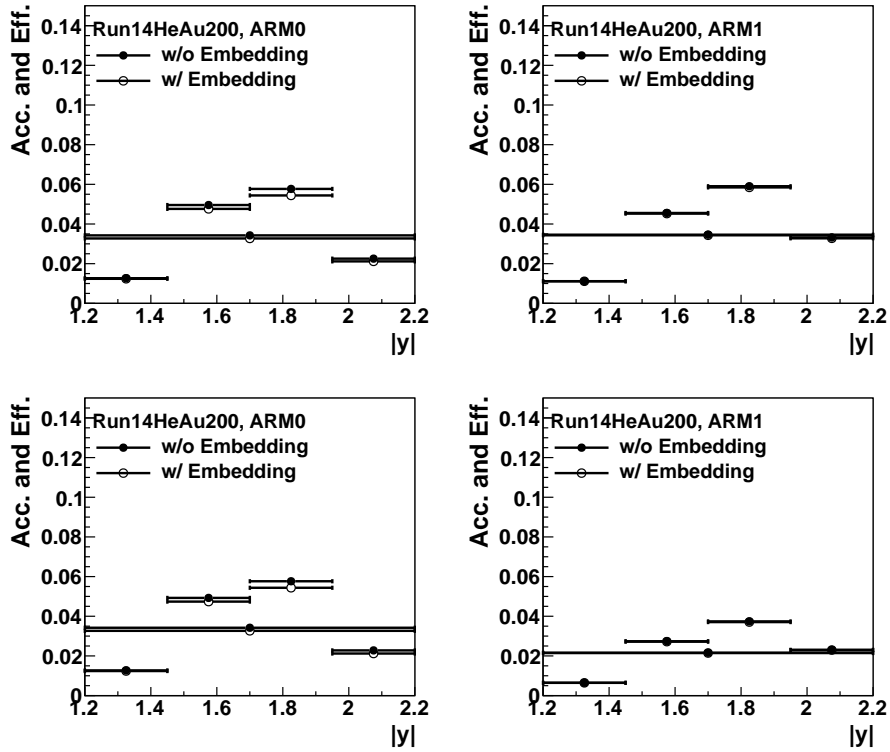


Figure 45: Acceptance and reconstruction efficiency of  $J/\psi$  as a function of rapidity in Run-14  $^3\text{He}+\text{Au}$ . Two sets of simulation have been prepared for different MuID efficiency. In  $\sim 70\%$  of runs, one panel in all MuID planes at the north arm are inefficient as shown in the bottom panel.

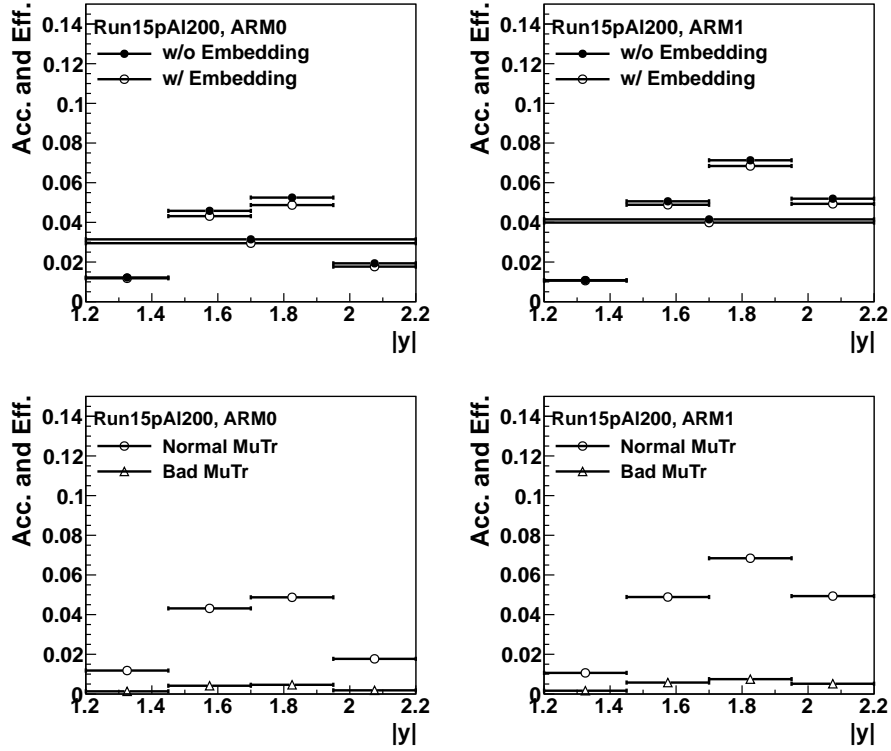


Figure 46: Acceptance and reconstruction efficiency of  $J/\psi$  as a function of rapidity in Run-15  $p+Al$ . Two sets of simulation have been prepared for different MuTr efficiency. In  $\sim 30\%$  of runs, half of MuTr at the south arm is off.

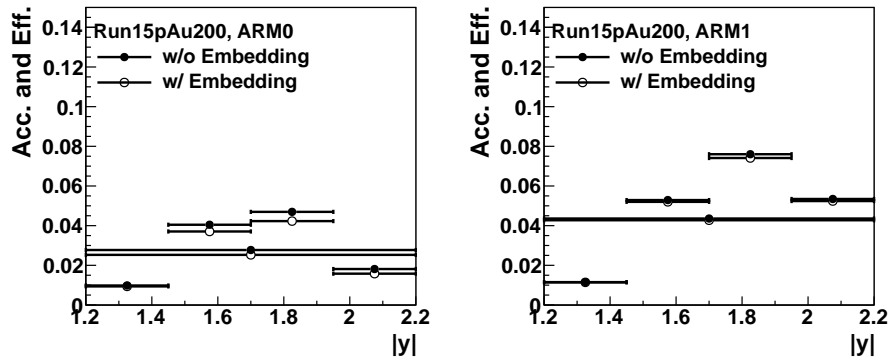


Figure 47: Acceptance and reconstruction efficiency of  $J/\psi$  as a function of rapidity in Run-15  $p+Au$ .

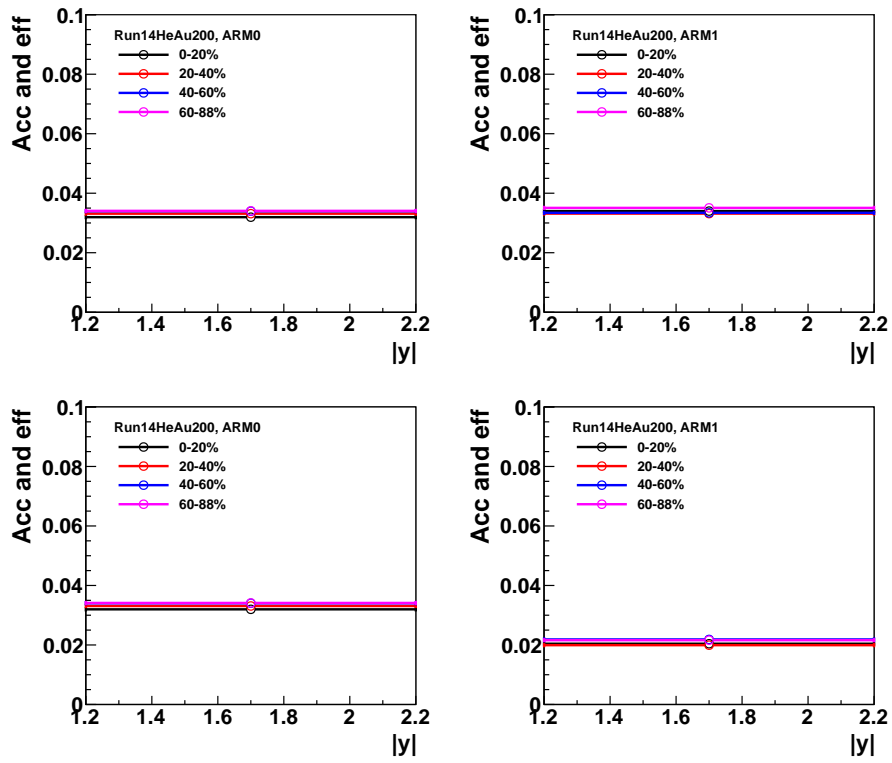


Figure 48: Centrality dependent acceptance and reconstruction efficiency in the integrated rapidity in two run groups of Run-14  $^3\text{He}+\text{Au}$ .

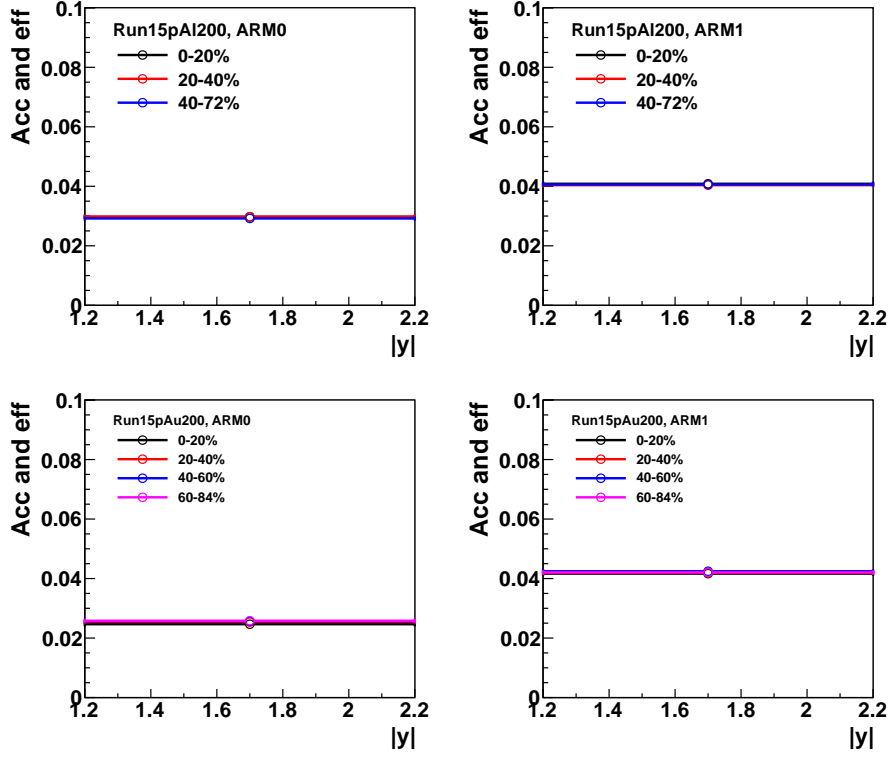


Figure 49: Centrality dependent acceptance and reconstruction efficiency in the integrated rapidity in Run-15  $p$ +Al (top), and  $p$ +Au (bottom).

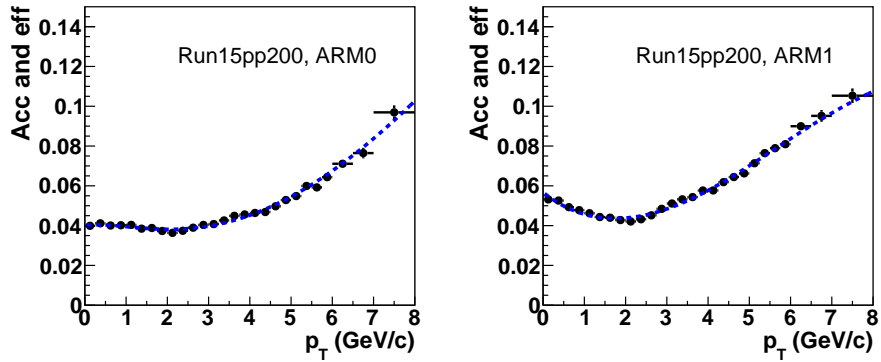


Figure 50: Acceptance and reconstruction efficiency as a function of  $p_T$  in Run-15  $p$ + $p$ .

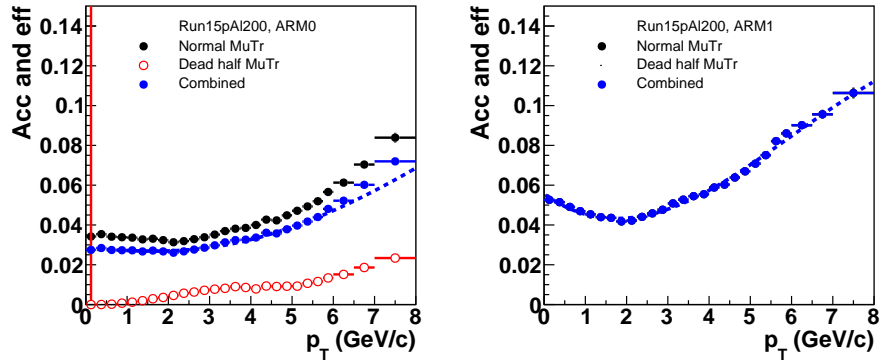


Figure 51: Acceptance and reconstruction efficiency as a function of  $p_T$  in Run-15  $p$ +Al.

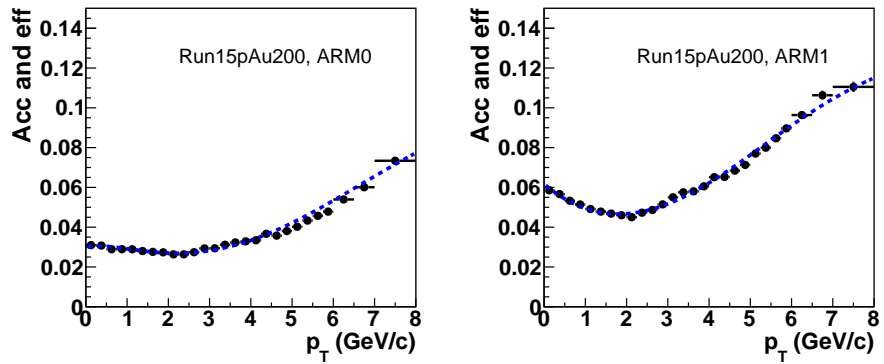


Figure 52: Acceptance and reconstruction efficiency as a function of  $p_T$  in Run-15  $p$ +Au.

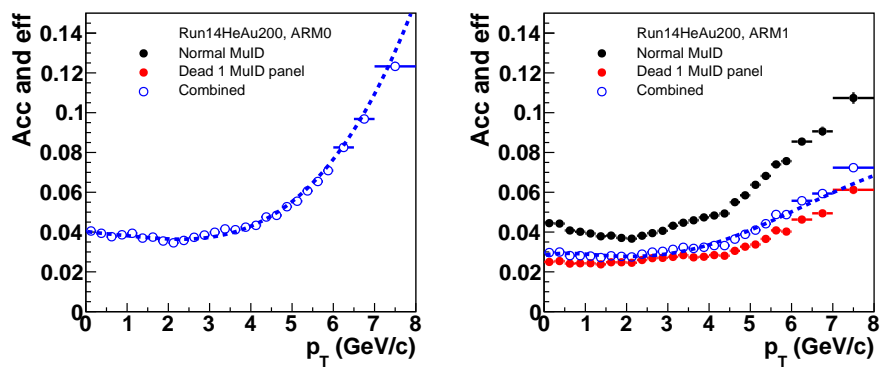


Figure 53: Acceptance and reconstruction efficiency as a function of  $p_T$  in Run-14  $^3\text{He}+\text{Au}$ .

### 3.8 Comparison between GEANT3 and GEANT4

In previous  $J/\psi$  analyses with the PHENIX muon arms, GEANT3 was used for simulation to evaluate acceptance and reconstruction efficiency. In recent muon arm analyses, GEANT4 interfaced with the G3toG4 has been used for detector simulation. Although material response of muons is not expected to be largely different between two GEANT versions, it's useful to quantify the difference. It's also important when comparing the  $J/\psi$  cross section in the new data set with GEANT4 with the published results (PPG104) with GEANT3. Figure 54 shows a comparison of the number of reconstructed dimuons as a function of  $p_T$  between GEANT3 and GEANT4 simulation with the same number of generated dimuons. Based on the ratio shown in the bottom panel, there's 10% less reconstructed dimuons in GEANT3 than that in GEANT4, so the corrected yield with GEANT4 simulation will be 10% smaller.

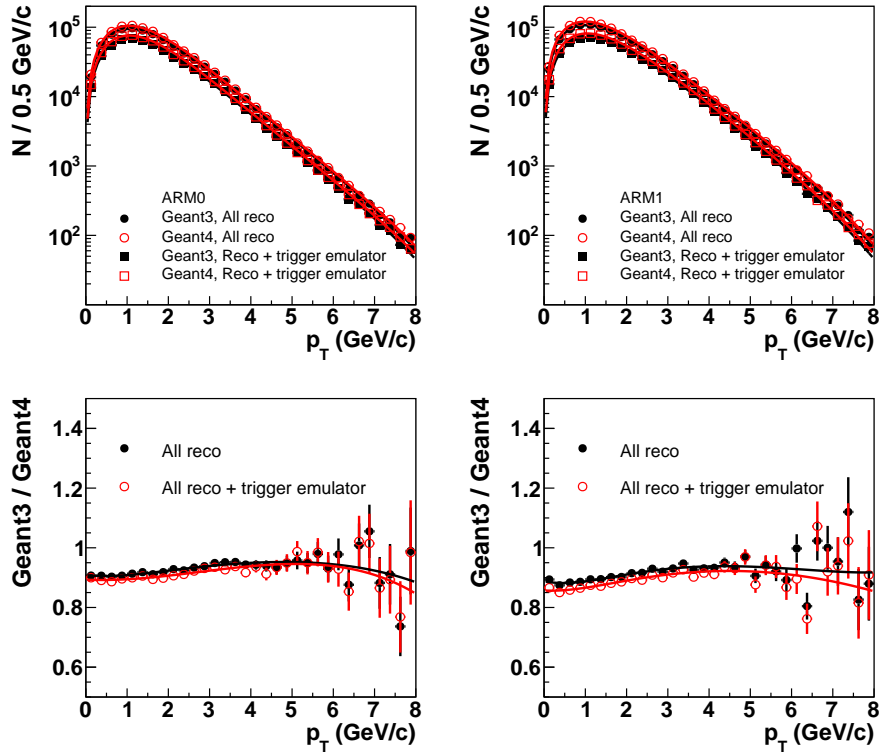


Figure 54: Comparison of the number of reconstructed dimuons between GEANT3 and GEANT4 simulations.

## 4 Fit

### 4.1 Cuts

Muon track candidates are identified using the muon arm cuts given in Tab. 1. To be considered in this analysis, tracks must reach at least the third gap in the MuID, have a good match with a MuID road, and have a reasonable chi2 value in the muon arm. Tracks that form a pair are required to pass through different octants, as typically occurs for actual charmonia dimuon decays. In addition, events are required to have a vertex position as determined by the BBC within 30 cm of the nominal vertex position, and events are required to have fired to 2D dimuon trigger.

Variable	Accepted Value
lastgap	$\geq 3$
DG0	$< 5\sigma$
DDG0	$< 5\sigma$
trchi2	$< 23$
octant cut	applied
idhits (hit pattern)	$> 14$
$ p_z $	$> 2 \text{ GeV}/c$
$ z_{BBC} $	$< 30 \text{ cm}$

Table 1: Cuts used in this analysis.

### 4.2 Like-sign Background

Using events which satisfied the same cuts used to find the unlike-sign dimuon invariant mass spectrum, the like-sign invariant mass spectrum was found for  $\mu^+\mu^+$  and  $\mu^-\mu^-$  pairs. The like-sign mass spectrum is normalized following the standard PHENIX methods:

$$Normalization_{l_s} = \frac{2\sqrt{N_{++}N_{--}}}{N_{++} + N_{--}}. \quad (1)$$

The properly normalized like-sign spectrum is fit with a function of the form

$$y = \frac{c}{(e^{-ax-bx^2} + x/d)^e}, \quad (2)$$

and included as a fixed background component in the total fit as described below.

### 4.3 Fit

A Crystal Ball function is used to represent the 1S and 2S peaks in the dimuon mass spectrum. Some info on the function can be found here: [Crystal Ball info](#)

The unlike sign dimuon spectrum is fit over the mass range  $2 < m_{\mu\mu} < 5$  GeV/ $c^2$  with the sum of the following components:

1. A Crystal Ball function representing the  $J/\psi$  peak. In the  $p + p$  data, these parameters describing the peak shape are allowed to float. When fitting the ion data, the  $n$  and  $\alpha$  parameters describing the low-side tail of the peak are fixed to what is found in  $p + p$ .
2. Another Crystal Ball function representing the  $\psi(2S)$  peak. The difference between the centroids of the  $J/\psi$  peak and this peak is set at the PDG value for the difference in mass between the two states, 589 MeV. This function is constrained to have a width of 1.15 times the width of the  $J/\psi$  peak, following expectations of the mass resolution in the muons arms as described in the muon arm NIM paper and PPG188. The Crystal Ball parameters  $\alpha$  and  $n$ , which describe the slope of the low mass tail, are also constrained to be the same as for the  $J/\psi$ , again following PPG188.
3. The uncorrelated (combinatorial) background is determined by a fit to the like-sign background, which is normalized as described above, and included as a fixed contribution in the total fit.
4. The correlated background from heavy-flavor decays and Drell-Yan pairs is represented by a function of the form given in Eq. 2.

An example of the fit to the rapidity integrated  $p + p$  data is shown in Fig. 55. The measured unlike-sign dimuon spectrum is the black data points, with a black line that represents the total fit function (the sum of all the individual components described in the preceding list). The gray shading around the black line represents the 90% CL around the fit. The peaks corresponding to the  $J/\psi$  and  $\psi(2S)$  states are shown in blue. The fixed background from like-sign events is shown in red points, with a fit that is a solid red line. The correlated background determined in the fitting procedure is shown in the green line. The total background (corresponding to a sum of the fixed like-sign event background plus the correlated background) is shown in red.

#### 4.4 Run-14 $^3\text{He} + \text{Au}$

Two example fits from the Run-14  $^3\text{He} + \text{Au}$  data are shown in Figs. 56 and 57. Note the difference in background between the South (Au-going) and North ( $^3\text{He}$ -going) directions. The combinatorial background determined from the like-sign dimuon spectrum is significantly larger in the South, although in the region of the  $J/\psi$  peak the signal/background ratio is still quite high.

#### 4.5 Run-15 $p + \text{Al}$

Two example fits from the Run-15  $p + \text{Al}$  data are shown in Figs. 58 and 59.

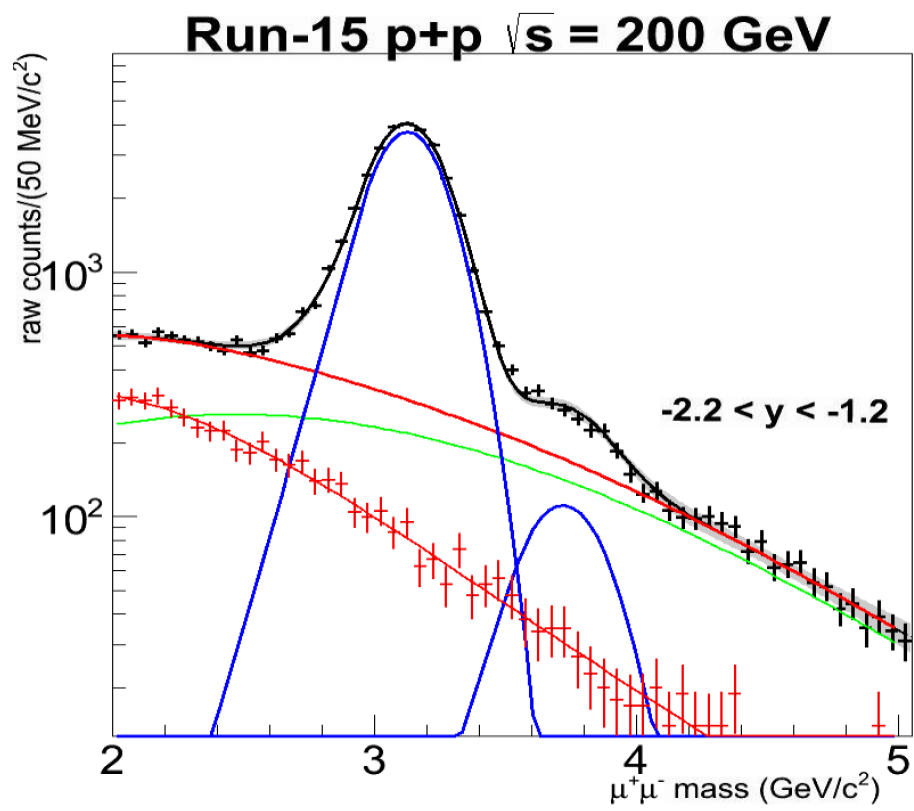


Figure 55: Fit to the dimuon  $p + p$  mass spectra for the South arm rapidity interval  $-2.2 < y < -1.2$ , prepared using the cuts described. In this fit,  $\chi^2/NDF = 65.99/50$ .

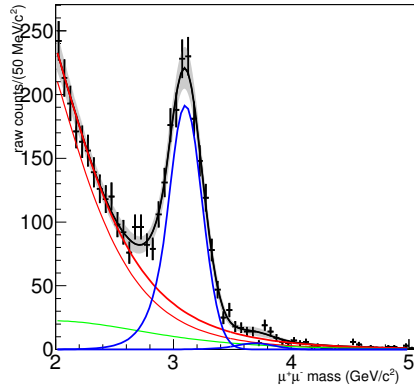


Figure 56: Fit to the dimuon  ${}^3\text{He}+\text{Au}$  mass spectra for the South arm rapidity interval  $-1.95 < y < 1.70$ , prepared using the cuts described.

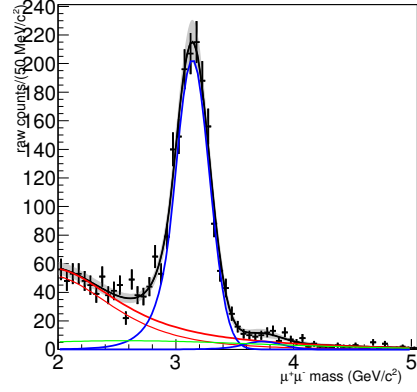


Figure 57: Fit to the dimuon  ${}^3\text{He}+\text{Au}$  mass spectra for the North arm rapidity interval  $1.70 < y < 1.95$ , prepared using the cuts described.

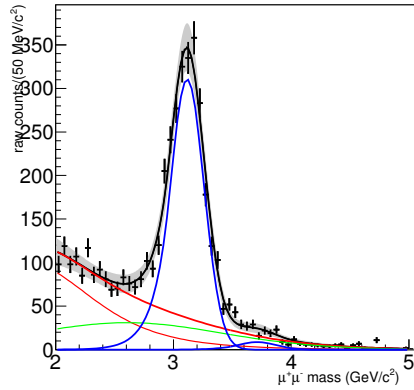


Figure 58: Fit to the dimuon  $p+\text{Al}$  mass spectra for the South arm rapidity interval  $-1.95 < y < 1.70$ , prepared using the cuts described.

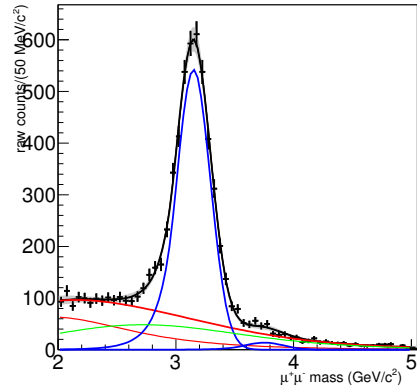


Figure 59: Fit to the dimuon  $p+\text{Al}$  mass spectra for the North arm rapidity interval  $1.70 < y < 1.95$ , prepared using the cuts described.

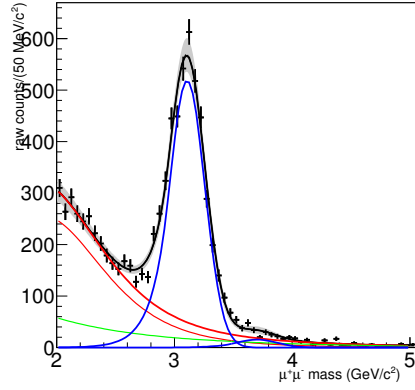


Figure 60: Fit to the dimuon  $p$ +Au mass spectra for the South arm rapidity interval  $-1.95 < y < 1.70$ , prepared using the cuts described.

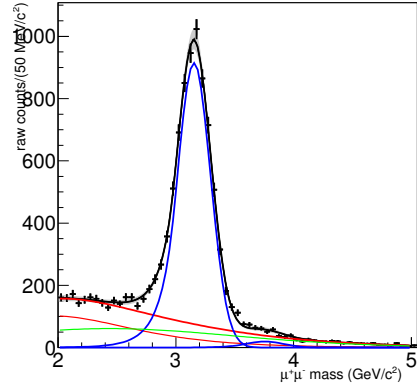


Figure 61: Fit to the dimuon  $p$ +Au mass spectra for the North arm rapidity interval  $1.70 < y < 1.95$ , prepared using the cuts described.

#### 4.6 Run-15 $p$ +Au

Two example fits from the Run-15  $p$ +Au data are shown in Figs. 60 and 61.

#### 4.7 Fit results

System	Rapidity	Extracted $J/\psi$ counts
${}^3\text{He}+\text{Au}$	-2.075	$484\pm 27$
	-1.825	$1454\pm 71$
	-1.575	$1455\pm 83$
	-1.325	$508\pm 28$
	1.325	$334\pm 21$
	1.575	$1318\pm 62$
	1.825	$1552\pm 56$
	2.075	$686\pm 29$
$p+\text{Au}$	-2.075	$973\pm 39$
	-1.825	$4138\pm 80$
	-1.575	$4910\pm 155$
	-1.325	$1521\pm 57$
	1.325	$1334\pm 60$
	1.575	$6464\pm 128$
	1.825	$6822\pm 136$
	2.075	$3793\pm 99$
$p+\text{Al}$	-2.075	$601\pm 47$
	-1.825	$2364\pm 107$
	-1.575	$2920\pm 234$
	-1.325	$682\pm 54$
	1.325	$843\pm 37$
	1.575	$3785\pm 95$
	1.825	$4125\pm 121$
	2.075	$2539\pm 87$
$p+p$	-2.075	$3017\pm 87$
	-1.825	$10918\pm 192$
	-1.575	$11341\pm 203$
	-1.325	$2907\pm 125$
	1.325	$1974\pm 58$
	1.575	$9997\pm 186$
	1.825	$11431\pm 192$
	2.075	$6554\pm 233$

Table 2: Summary of  $J/\psi$  counts measured in each rapidity bin in the Run-14  ${}^3\text{He}+\text{Au}$  and Run-15  $p+p,\text{Al},\text{Au}$  data.

${}^3\text{He}+\text{Au}$ centrality	Backward Rapidity	Forward Rapidity
60-88%	$395\pm 24$	$432\pm 36$
40-60%	$766\pm 33$	$694\pm 38$
20-40%	$1116\pm 49$	$1182\pm 40$
0-20%	$1837\pm 83$	$1517\pm 64$
Min Bias	$3987\pm 118$	$3825\pm 91$

Table 3: Centrality dependence of  $J/\psi$  counts measured at forward and backward rapidity in Run-14  ${}^3\text{He}+\text{Au}$ .

$p$ +Au centrality	Backward Rapidity	Forward Rapidity
60-84%	1438±43	3146±81
40-60%	2026±98	4122±152
20-40%	3082±105	5077±120
0-20%	5002±95	6026±138
Min Bias	11602±193 18194	224

Table 4: Centrality dependence of  $J/\psi$  counts measured at forward and backward rapidity in Run-15  $p$ +Au.

$p$ +Al centrality	Backward Rapidity	Forward Rapidity
40-72%	1968±74	3610±109
20-40%	1821±84	3257±95
0-20%	3025±129	4289±118
Min Bias	6567±206	11085±190

Table 5: Centrality dependence of  $J/\psi$  counts measured at forward and backward rapidity in Run-15  $p$ +Al.

$p + p$	Backward Rapidity	Forward Rapidity
	28207±282	29399±279

Table 6:  $J/\psi$  counts measured at forward and backward rapidity in Run-15  $p+p$  over the rapidity intervals  $1.2 < |y| < 2.2$ .

## 5 Systematic uncertainty

### 5.1 Fit

Here we determine systematic uncertainties on the  $J/\psi$  yields extracted from fitting the data. First we consider the uncertainty on the uncorrelated background, which is included in the fit as a fixed contribution that is determined from the like-sign dimuon data. As previously described, this background is represented by a fit to the like-sign data. We vary this background by changing the normalization parameter of the fit by  $\pm 1\sigma_N$ , where  $\sigma_N$  is the uncertainty on that parameter as determined by the fit to the like sign data. The systematic uncertainty due to the uncertainty on the background is found by averaging the differences between the upper and lower bounds. As expected, these uncertainties are small for  $p + p$  data which has a small background contribution that is well constrained by a high-statistics dataset, and generally larger in the South (ion-going) arm where backgrounds are larger and datasets are smaller.

System, Arm	Like-sign bg variation	$J/\psi(1s)$ counts	Deviation from central value (percent)
$p + p$ , N	nominal	29399	N/A
$p + p$ , S	nominal	28207	N/A
$p + p$ , N	$+1\sigma_N$	29240	0.5%
$p + p$ , S	$+1\sigma_N$	28171	0.1%
$p + p$ , N	$-1\sigma_N$	29572	0.6%
$p + p$ , S	$-1\sigma_N$		1.6%
$p + \text{Al}$ , N	nominal	11085	N/A
$p + \text{Al}$ , S	nominal	6567	N/A
$p + \text{Al}$ , N	$+1\sigma_N$	11204	1.1%
$p + \text{Al}$ , S	$+1\sigma_N$	6872	4.6%
$p + \text{Al}$ , N	$-1\sigma_N$	11135	0.4%
$p + \text{Al}$ , S	$-1\sigma_N$	6844	4.2%
$p + \text{Au}$ , N	nominal	18194	N/A
$p + \text{Au}$ , S	nominal	11602	N/A
$p + \text{Au}$ , N	$+1\sigma_N$	18199	0.03%
$p + \text{Au}$ , S	$+1\sigma_N$	11631	0.3%
$p + \text{Au}$ , N	$-1\sigma_N$	18268	0.4%
$p + \text{Au}$ , S	$-1\sigma_N$	11596	0.1%
$^3\text{He} + \text{Au}$ , N	nominal	3825	N/A
$^3\text{He} + \text{Au}$ , S	nominal	3987	N/A
$^3\text{He} + \text{Au}$ , N	$+1\sigma_N$	3893	1.8%
$^3\text{He} + \text{Au}$ , S	$+1\sigma_N$	4133	3.6%
$^3\text{He} + \text{Au}$ , N	$-1\sigma_N$	3834	0.2%
$^3\text{He} + \text{Au}$ , S	$-1\sigma_N$	3920	1.7%

Table 7: Summary of changes in the extracted  $J/\psi$  yield when adjusting the normalization of the like-sign background in the fit.

As previously discussed, the Crystal Ball parameters  $n$  and  $\alpha$  are allowed to float when fitting the  $p+p$  data. Therefore, the uncertainties  $\sigma_n$  and  $\sigma_\alpha$  on those parameters are included in the fit's total covariance matrix and reflected in the statistical uncertainty on the extracted  $J/\psi$  yields. However, to constrain the  $J/\psi$  line shape, these parameters are fixed to the values determined by the  $p+p$  fit when performing fits on the p+A data. Here we vary those fit parameters by  $\pm 1\sigma_n$  and  $\pm 1\sigma_\alpha$ , and assign a systematic uncertainty based on the variation in the extracted yields.

While performing this task, we found that some of the fits would not converge with the  $n$  parameter at its upper limit. In these cases, we use the yield determined with the lower limit as the total systematic uncertainty, rather than an average of the lower and upper. In all cases where the uncertainties are less than 1%, they are rounded up to 1%.

System, Arm	$n$ parameter variation	$J/\psi(1s)$ counts	Deviation from central value (percent)
$p+Al$ , N	nominal	11085	N/A
$p+Al$ , S	nominal	6567	N/A
$p+Al$ , N	$+1\sigma_n$	11412	2.9%
$p+Al$ , S	$+1\sigma_n$	6557	0.1%
$p+Al$ , N	$-1\sigma_n$	11383	2.7%
$p+Al$ , S	$-1\sigma_n$	6594	0.4%
$p+Au$ , N	nominal	18194	N/A
$p+Au$ , S	nominal	11602	N/A
$p+Au$ , N	$+1\sigma_n$	did not converge	XX%
$p+Au$ , S	$+1\sigma_n$	11542	0.5%
$p+Au$ , N	$-1\sigma_n$	18628	2.4%
$p+Au$ , S	$-1\sigma_n$	11664	0.5%
$^3He+Au$ , N	nominal	3825	N/A
$^3He+Au$ , S	nominal	3987	N/A
$^3He+Au$ , N	$+1\sigma_n$	did not converge	XX%
$^3He+Au$ , S	$+1\sigma_n$	3960	0.7%
$^3He+Au$ , N	$-1\sigma_n$	3895	xx%
$^3He+Au$ , S	$-1\sigma_n$	4015	0.7%

Table 8: Summary of changes in the extracted  $J/\psi$  yield when adjusting the Crystal Ball parameter  $n$  describing the  $J/\psi$  line shape within uncertainties.

System, Arm	$\alpha$ parameter variation	$J/\psi(1s)$ counts	Deviation from central value (percent)
$p$ +Al, N	nominal	11085	N/A
$p$ +Al, S	nominal	6567	N/A
$p$ +Al, N	$+1\sigma_\alpha$	10993	0.8%
$p$ +Al, S	$+1\sigma_\alpha$	6514	0.8%
$p$ +Al, N	$-1\sigma_\alpha$	11152	0.6%
$p$ +Al, S	$-1\sigma_\alpha$	6612	0.7%
$p$ +Au, N	nominal	18194	N/A
$p$ +Au, S	nominal	11602	N/A
$p$ +Au, N	$+1\sigma_\alpha$	18073	0.6%
$p$ +Au, S	$+1\sigma_\alpha$	11594	0.1%
$p$ +Au, N	$-1\sigma_\alpha$	18279	0.5%
$p$ +Au, S	$-1\sigma_\alpha$	11630	0.2%
$^3\text{He}$ +Au, N	nominal	3825	N/A
$^3\text{He}$ +Au, S	nominal	3987	N/A
$^3\text{He}$ +Au, N	$+1\sigma_\alpha$	3806	xx%
$^3\text{He}$ +Au, S	$+1\sigma_\alpha$	3983	0.1%
$^3\text{He}$ +Au, N	$-1\sigma_\alpha$	3840	0.4%
$^3\text{He}$ +Au, S	$-1\sigma_\alpha$	3998	0.1%

Table 9: Summary of changes in the extracted  $J/\psi$  yield when adjusting the Crystal Ball parameter  $\alpha$  describing the  $J/\psi$  line shape within uncertainties.

Uncertainty Source	North arm	South arm
Like-sign bg normalization	1%	4.4%
$n$ parameter	2.8%	1%
$\alpha$ parameter	1%	1%

Table 10: Summary of systematic uncertainties from fits on the  $p$ +Al data.

Uncertainty Source	North arm	South arm
Like-sign bg normalization	1%	1%
$n$ parameter	2.4%	1%
$\alpha$ parameter	1%	1%

Table 11: Summary of systematic uncertainties from fits on the  $p$ +Au data.

Uncertainty Source	North arm	South arm
Like-sign bg normalization	1%	2.7%
$n$ parameter	2.4%	1%
$\alpha$ parameter	1%	1%

Table 12: Summary of systematic uncertainties from fits on the  $^3\text{He}$ +Au data.

## 5.2 Run-to-run variation

In order to consider a systematic uncertainty from variation of detector performance during the data taking period, the difference between two groups of run (low and high BBCLL1 trigger rates) shown in Figs. 28, 30, and 32 are assigned to this systematic uncertainty.

System, Arm	Relative uncertainty
$p+p$ , S	4.7%
$p+p$ , N	4.0%
${}^3\text{He}+\text{Au}$ , S	5.0%
${}^3\text{He}+\text{Au}$ , N	1.5%
$p+\text{Al}$ , S	3.3%
$p+\text{Al}$ , N	2.8%
$p+\text{Au}$ , S	3.5%
$p+\text{Au}$ , N	1.6%

## 5.3 Acceptance and reconstruction efficiency

The systematic uncertainty on acceptance and reconstruction efficiency is evaluated with two sources. One is matching MuTr  $\varphi$  acceptance, and another is from variation of initial  $p_T$  and  $y$  distribution used for simulation. Figures 62, 63, 64, and 65 show comparisons of MuTr  $\varphi$  distributions between simulation and data in all collision systems. In case of the systematic uncertainty due to initial input distributions, it showed  $\sim 4\%$  variation is shown in the rapidity bin of  $1.2 < |y| < 1.45$  and  $< 1\%$  variation in the other rapidity bins.

System, Arm	Relative uncertainty due to MuTr $\varphi$ matching	Relative uncertainty due to initial shapes
$p+p$ , S	5.0%	2%
$p+p$ , N	5.8%	2%
${}^3\text{He}+\text{Au}$ , S	2.5%	2%
${}^3\text{He}+\text{Au}$ , N	3.1%	2%
$p+\text{Al}$ , S	3.3%	2%
$p+\text{Al}$ , N	3.6%	2%
$p+\text{Au}$ , S	4.0%	2%
$p+\text{Au}$ , N	3.4%	2%

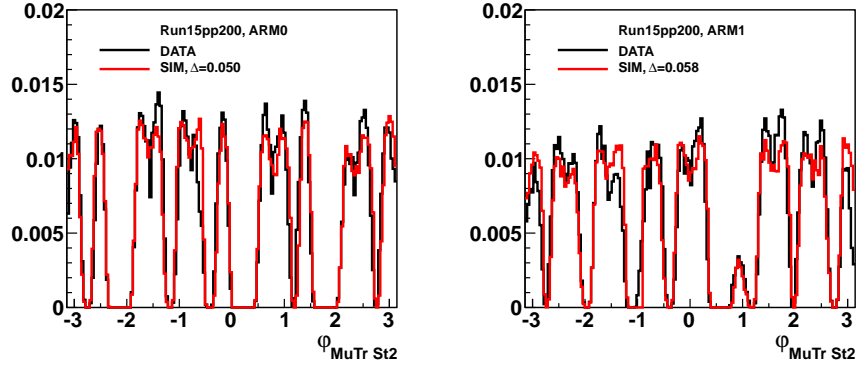


Figure 62: Comparison of MuTr  $\varphi$  distribution between simulation and data in Run-15  $p+p$ .

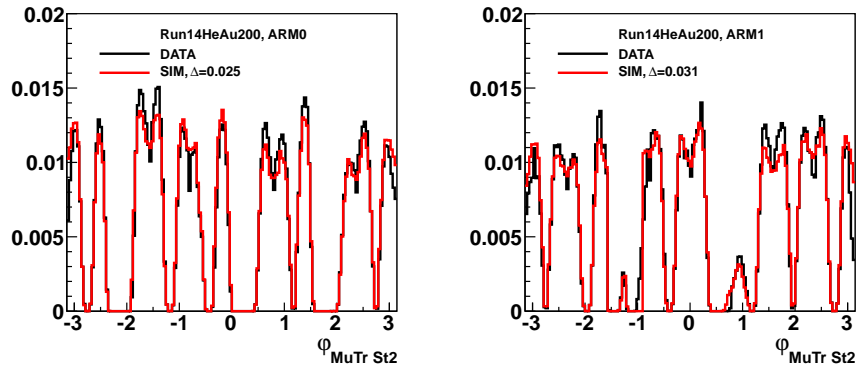


Figure 63: Comparison of MuTr  $\varphi$  distribution between simulation and data in Run-14  ${}^3\text{He}+\text{Au}$ .

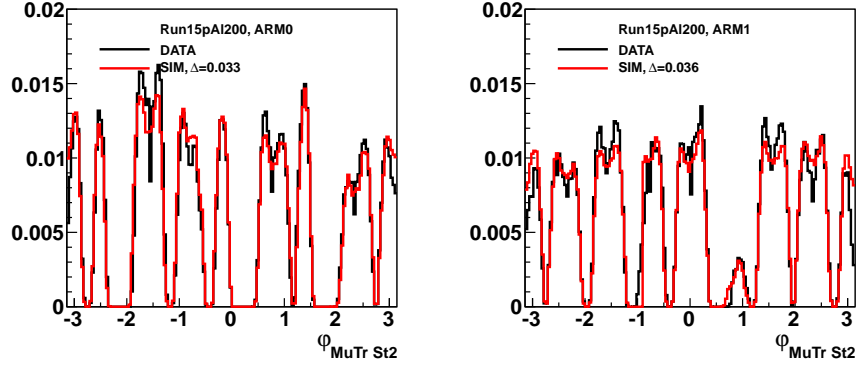


Figure 64: Comparison of MuTr  $\varphi$  distribution between simulation and data in Run-15  $p+Al$ .

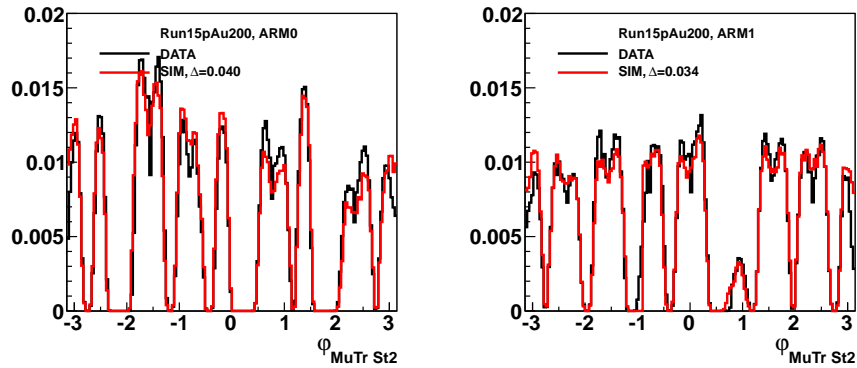


Figure 65: Comparison of MuTr  $\varphi$  distribution between simulation and data in Run-15  $p+Au$ .

## 5.4 Trigger efficiency

The systematic uncertainty on the MuID-2D trigger efficiency has been evaluated by taking the difference between the data driven method and the trigger emulator in the integrated rapidity bin as shown in Figs. 66, 67, 68, and 69. The systematic uncertainty as a function of  $p_T$  in the integrated rapidity is about 1–5% as shown in the bottom panel of 42, 39, 40, and 41.

System, Arm	Relative uncertainty
$p+p$ , S	1.0–7.3%
$p+p$ , N	1.0–5.4%
$^3\text{He}+\text{Au}$ , S	1.0–5.0%
$^3\text{He}+\text{Au}$ , N	1.0–4.1%
$p+\text{Al}$ , S	1.0–11.8%
$p+\text{Al}$ , N	1.0–5.6%
$p+\text{Au}$ , S	1.0–8.7%
$p+\text{Au}$ , N	1.0–5.4%

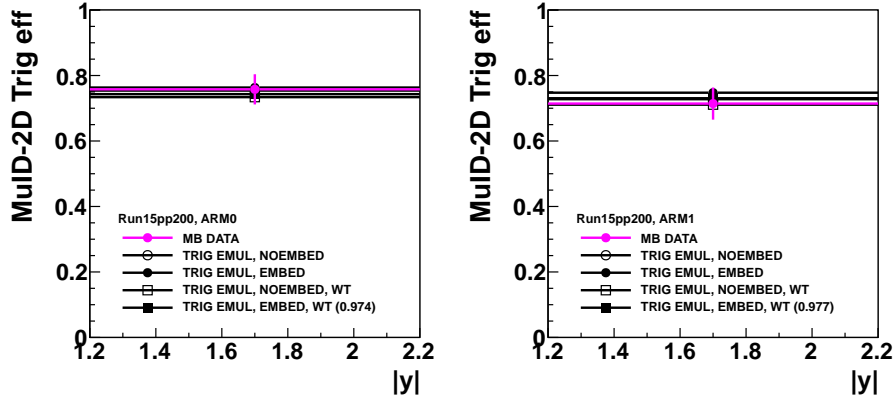


Figure 66: Comparison of MuID-2D trigger efficiency between simulation and data in Run-15  $p+p$ .

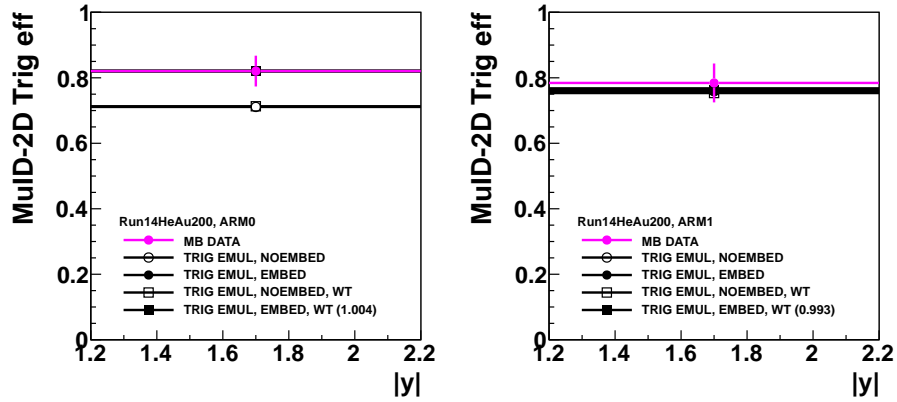


Figure 67: Comparison of MuID-2D trigger efficiency between simulation and data in Run-14  $^3\text{He}+\text{Au}$ .

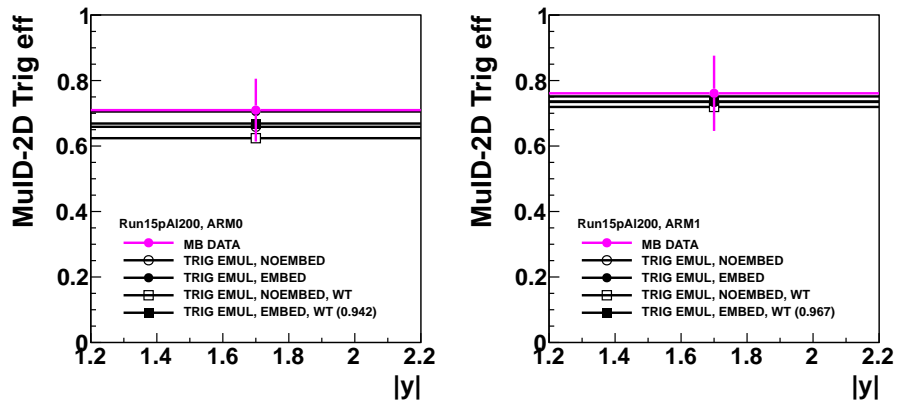


Figure 68: Comparison of MuID-2D trigger efficiency between simulation and data in Run-15  $p+\text{Al}$ .

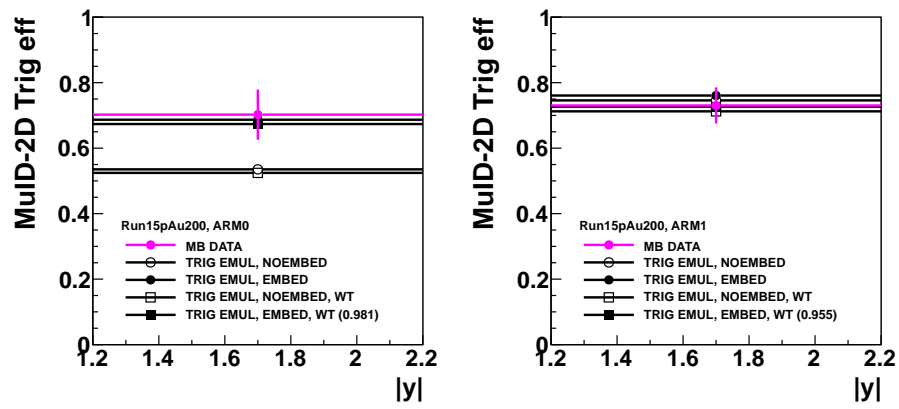


Figure 69: Comparison of MuID-2D trigger efficiency between simulation and data in Run-15  $p$ +Au.

## 5.5 $J/\psi$ polarization

Depending on the sign and magnitude of  $J/\psi$  polarization, the acceptance of  $J/\psi$  is expected to be varied significantly with a limited detector coverage. This effect can be studied by the GSU dimuon generator. Figure 71 shows correlation of  $\eta$  of single muons from  $J/\psi$  decay in three cases of  $J/\psi$  polarization, unpolarized (top),  $\lambda = +1$  (middle), and  $\lambda = -1$  (bottom), in various  $J/\psi$  rapidity bins. A clear difference is seen in the plot, and it's more visible in 1D distributions of single muon  $\eta$  shown in Fig. 70.

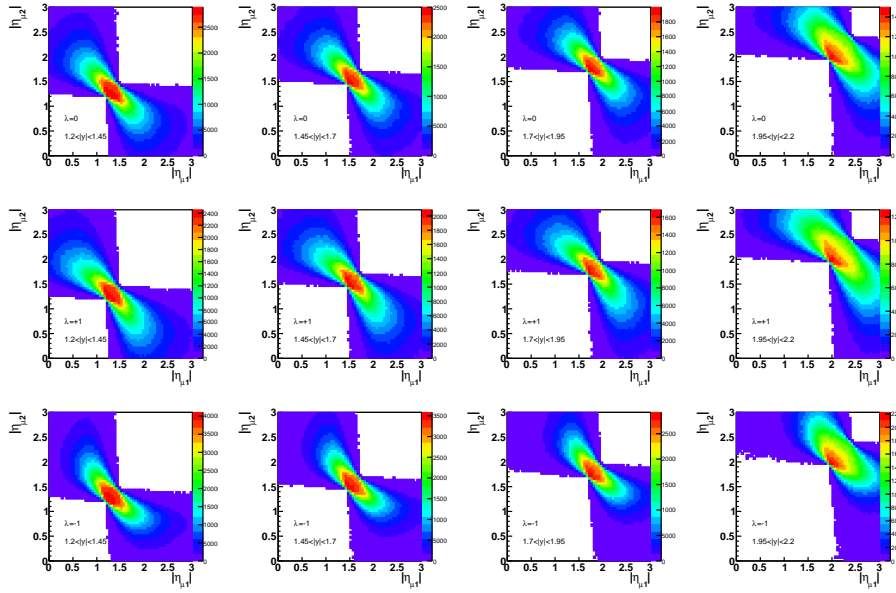


Figure 70: Comparison of correlation of  $\eta$  from  $J/\psi$  decay among three cases of polarization in various  $J/\psi$  rapidity bins.

Figure 72 shows a comparison of acceptance and efficiency as a function of  $J/\psi$  rapidity, and Fig 73 shows a same comparison as a function of  $J/\psi$   $p_T$ . As there's no precise measurement of  $J/\psi$  polarization in  $p+p$  collisions at  $\sqrt{s} = 200$  GeV, a maximum polarization  $\lambda = +1$  and  $\lambda = -1$  is assumed to evaluate systematic uncertainty. The default acceptance and efficiency is evaluated with PYTHIA8 which is the case of unpolarized  $J/\psi$ , and the maximum deviation divide by  $\sqrt{12}$  is assigned to  $1\sigma$  systematic uncertainty shown in the bottom panel of Fig. 73.

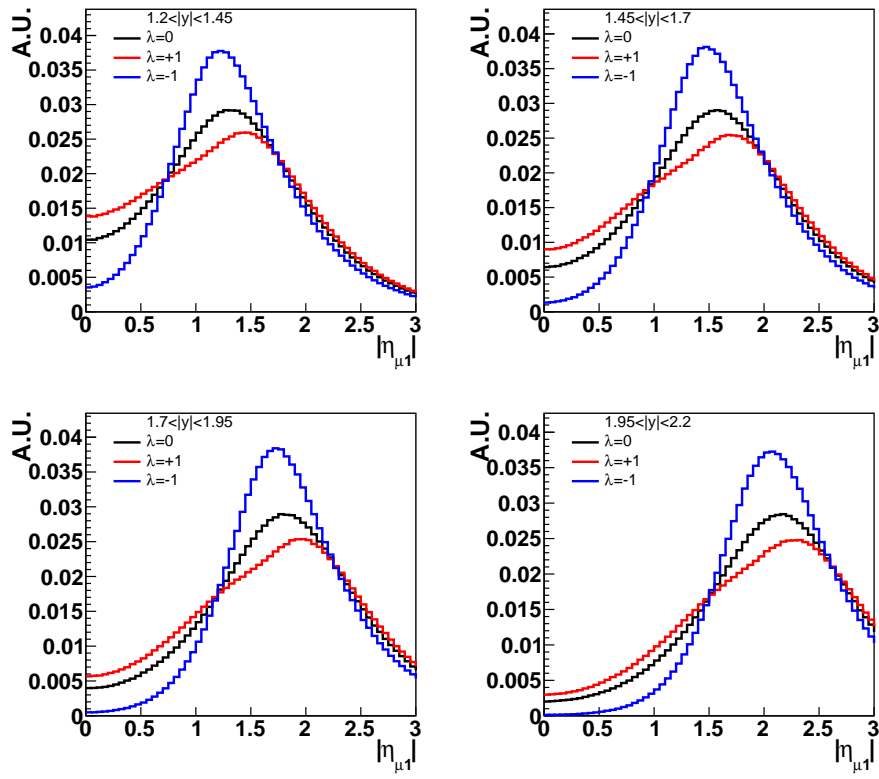


Figure 71: Comparison of  $\eta$  distributions from  $J/\psi$  decay among three cases of polarization in various  $J/\psi$  rapidity bins.

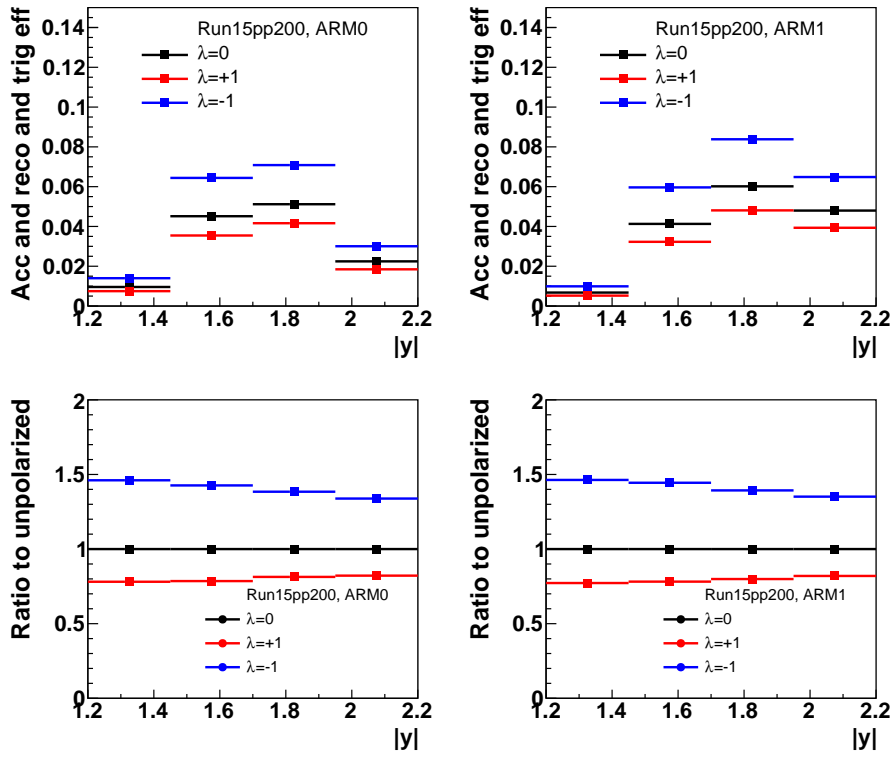


Figure 72: Comparison of acceptance and efficiency as a function of  $J/\psi$  rapidity.

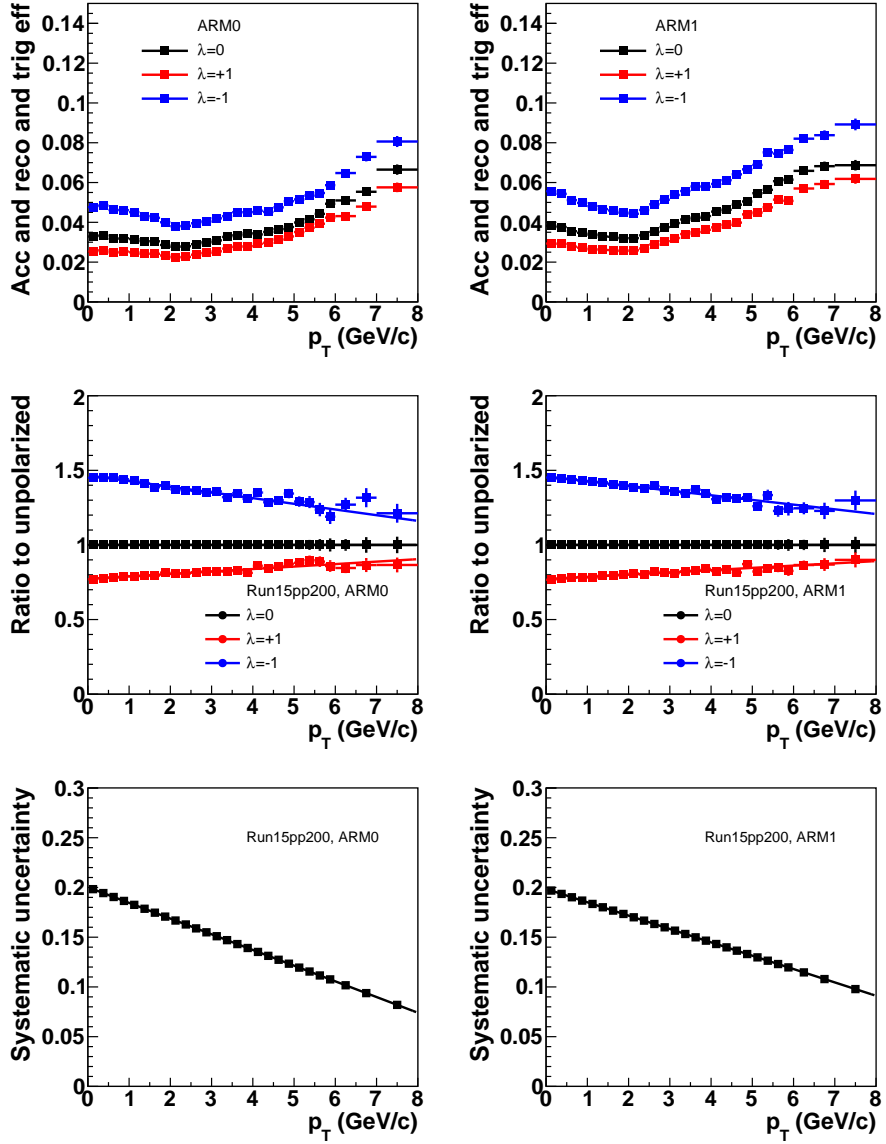


Figure 73: Comparison of acceptance and efficiency as a function of  $J/\psi$  rapidity and related systematic uncertainty.

## 6 Results

### 6.1 $dN/dy$ of $J/\psi$

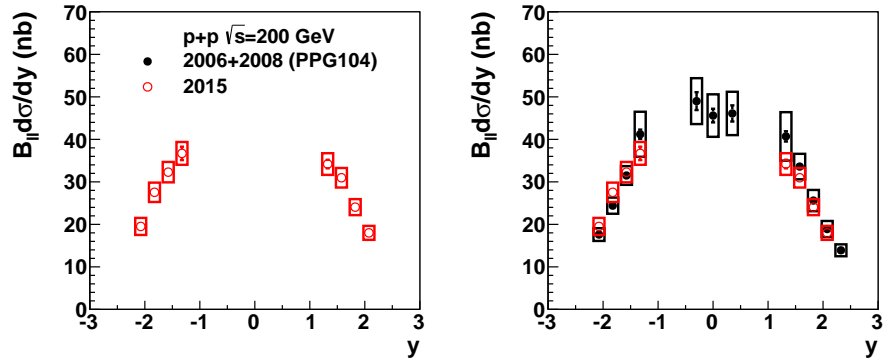


Figure 74:  $B_{ud}d\sigma/dy$  of as a function of rapidity  $J/\psi$  in Run-15  $p+p$  (left) and comparison with the PPG104 results. Bars (boxes) around data points represent statistical (systematic) uncertainties.

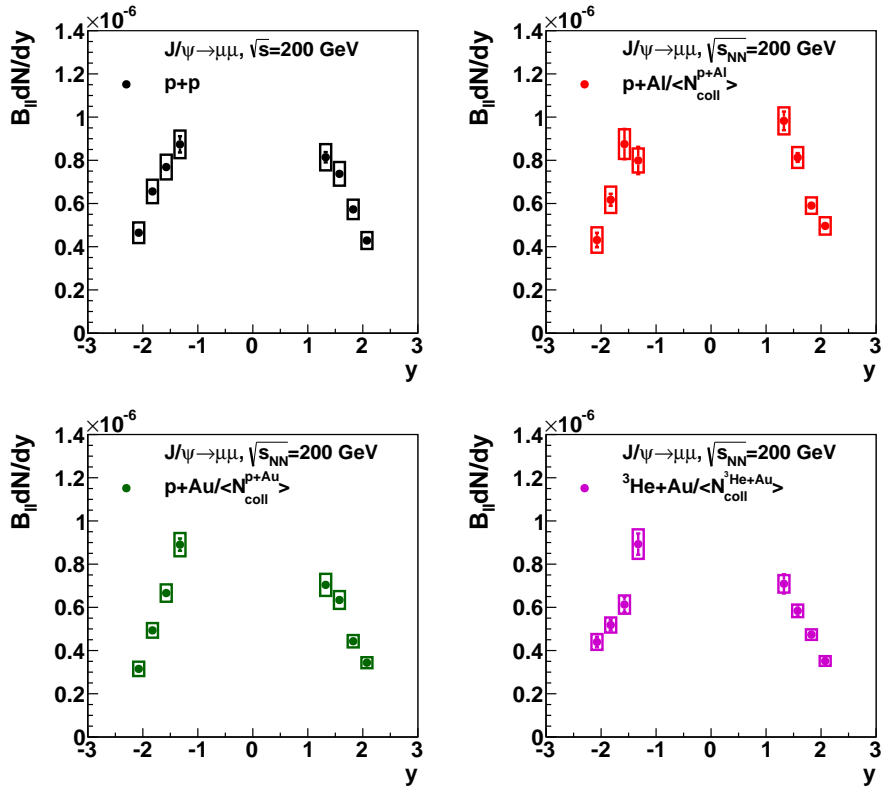


Figure 75:  $B_{\parallel} dN/dy$  of  $J/\psi$  as a function of rapidity in Run-15  $p+p$  (top left),  $p+Al$  (top right),  $p+Au$  (bottom left), and Run-14  ${}^3\text{He}+Au$  (bottom right). The results in  $p+Al$ ,  $p+Au$ , and  ${}^3\text{He}+Au$  are scaled with the  $\langle N_{coll} \rangle$  for each system. Bars (boxes) around data points represent statistical (systematic) uncertainties.

## 6.2 $R_{pA}$ of $J/\psi$

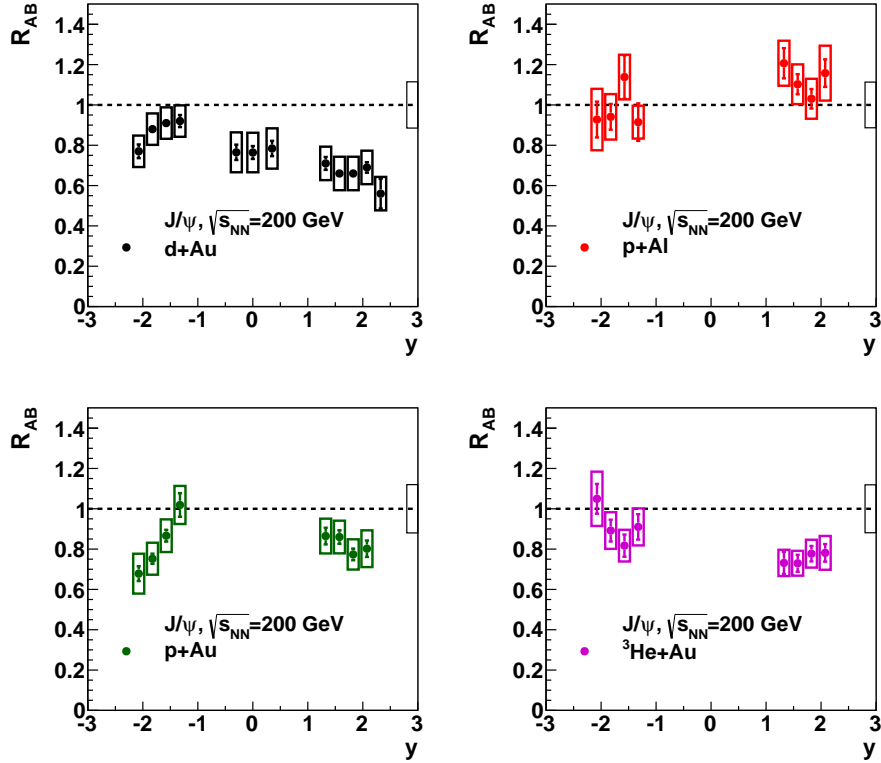


Figure 76:  $R_{AB}$  of  $J/\psi$  as a function of rapidity in  $d+Au$  (top left),  $p+Al$  (top right),  $p+Au$  (bottom left), and Run-14  ${}^3\text{He}+Au$  (bottom right). Bars (boxes) around data points represent point-to-point uncorrelated (correlated) uncertainties.

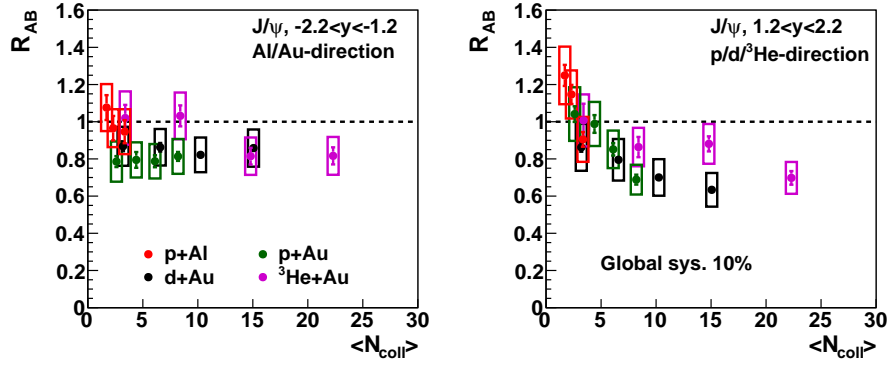


Figure 77:  $R_{AB}$  of  $J/\psi$  as a function of  $\langle N_{coll} \rangle$  at backward (left) and forward rapidity. Bars (boxes) around data points represent point-to-point uncorrelated (correlated) uncertainties.